AD-A060 836 NAVAL RESEARCH LAB WASHINGTON D C F/G 20/1
EVALUATION OF THE RELATIVE IMPORTANCE OF CIRCUMFERENTIAL OR CRE--ETC(U)
SEP 78 L R DRAGONETTE
UNCLASSIFIED NRL-8216 NL

1 OF 1
AD
A060 836

END
DATE
FILMED
1-79
DDC

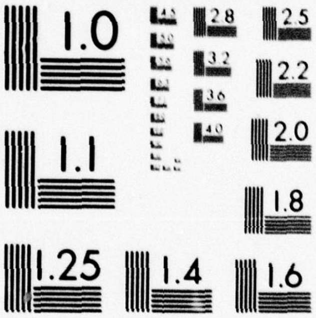

MICROCOPY RESOLUTION TEST CHART

LEVEL II

(12) B.S.

NRL Report 8216

(6)

Evaluation of the Relative Importance of Circumferential or Creeping Waves in the Acoustic Scattering from Rigid and Elastic Solid Cylinders and from Cylindrical Shells.

(10) LOUIS R. DRAGONETTE

Physical Acoustics Division
Acoustics Division

(9) Interim rept.,

(14) NRL-8216

(11) 22 Sept[redacted]978

(12) 68p.

(16) F11121

(17)

NAVAL RESEARCH LABORATORY
Washington, D.C.

251 950

REPORT DOCUMENTATION PAGE	READ INSTRUCTIONS BEFORE COMPLETING FORM
1. REPORT NUMBER NRL Report 8216 ✓	2. GOVT ACCESSION NO.
	3. RECIPIENT'S CATALOG NUMBER
4. TITLE (and Subtitle) EVALUATION OF THE RELATIVE IMPORTANCE OF CIRCUMFERENTIAL OR CREEPING WAVES IN THE ACOUSTIC SCATTERING FROM RIGID AND ELASTIC SOLID CYLINDERS AND FROM CYLINDRICAL SHELLS	5. TYPE OF REPORT & PERIOD COVERED Interim report on a continuing NRL Problem 6. PERFORMING ORG. REPORT NUMBER
7. AUTHOR(s) Louis R. Dragonette	8. CONTRACT OR GRANT NUMBER(s) 62711 N
9. PERFORMING ORGANIZATION NAME AND ADDRESS Naval Research Laboratory ✓ Washington, D. C. 20375	10. PROGRAM ELEMENT, PROJECT, TASK AREA & WORK UNIT NUMBERS NRL Problem S01-84 -NRL Project SF11-121
11. CONTROLLING OFFICE NAME AND ADDRESS Department of the Navy Naval Sea Systems Command Washington, D. C. 20362	12. REPORT DATE September 22, 1978 13. NUMBER OF PAGES 70
14. MONITORING AGENCY NAME & ADDRESS (if different from Controlling Office)	15. SECURITY CLASS. (of this report) Unclassified 15a. DECLASSIFICATION/DOWNGRADING SCHEDULE

16. DISTRIBUTION STATEMENT (of this Report)

Approved for public release; distribution unlimited.

17. DISTRIBUTION STATEMENT (of the abstract entered in Block 20, if different from Report)

18. SUPPLEMENTARY NOTES

19. KEY WORDS (Continue on reverse side if necessary and identify by block number)

Acoustics	Circumferential waves
Underwater acoustics	Creeping waves
Theory	
Sound scattering	

20. ABSTRACT (Continue on reverse side if necessary and identify by block number)

The relationship is determined between predicted circumferential waves on cylinders and the *normal-mode series solution for the* acoustic scattering by submerged metal cylinders. Specific circumferential waves are linked to the free modes of vibration of the cylinder, and this identification is used to experimentally detect the Rayleigh surface wave at low ka. Circumferential waves on thin cylindrical shells are demonstrated to closely follow prediction based on Lamb theory for flat plates.

DD FORM 1 JAN 73 1473 EDITION OF 1 NOV 65 IS OBSOLETE
S/N 0102-014-6601

CONTENTS

EVALUATION OF THE RELATIVE IMPORTANCE OF CIRCUMFERENTIAL OR CREEPING WAVES IN THE ACOUSTIC SCATTERING FROM RIGID AND ELASTIC SOLID CYLINDERS AND FROM CYLINDRICAL SHELLS

I. INTRODUCTION

A. Normal mode series solution and experimental verification

Theoretical solutions to the problem of the scattering of sound by rigid, immovable cylinders, nonrigid cylinders in a fluid medium, and small cylindrical obstacles in a solid medium were formulated by Rayleigh [1]. The solutions he presented described geometries in which the diameters of the cylinders were small compared to the acoustic wavelength in the surrounding medium, although he outlined a more general method for finding the solution for larger diameter cylinders in terms of cylindrical harmonics. This method, called the harmonic series or the Rayleigh series method of solving acoustic scattering problems is in theory applicable to targets whose shape conforms to any of the eleven separable coordinate systems. In practice it has been extensively applied only to scattering from spherical and infinite cylindrical geometries, since cylindrical and spherical harmonics are readily available. Solutions to the problems of the scattering from rigid cylinders and rigid spheres which have radii up to the order of a wavelength ($ka \simeq 6$) were given by Morse, [2]; here $ka = 2\pi a/\lambda$, a is the radius of the scatterer, and λ is the acoustic wavelength in water. Exact solutions to the scattering of a plane sound wave by homogeneous, isotropic cylinders and spheres capable of supporting both shear and compressional waves (elastic scatterers) were first given by Faran [3], who obtained expressions in terms of a normal mode series. Faran presented comparisons of computed bistatic patterns and experimental measurements at $ka = 5$. Extensions of the normal mode calculations to higher ka [4,5] and experimental measurements to determine the degree to which the normal mode theory and experiment agreed, over a broad ka range, were first made on solid elastic spheres and spherical shells [6-9]. Hickling [4] was the first to make extensive use of a digital computer to evaluate the normal mode series expressions, although his computations were hampered by the slow convergence of the haromonic series solution, which led to computation difficulties with the computers available at that time. Hickling gave computed curves that describe the steady state backscattered pressure vs ka, which results when the target is a solid elastic sphere in water. The computations in his work ranged generally from $0 < ka \leqslant 30$, and he extended the formulation to include the scattering of incident spherical as well as incident plane waves. He also included both near field and far field formulations. The results presented by Hickling are given in terms of a normalized, reflected pressure variable called the form function, f_∞. This dimensionless quantity is obtained by normalizing the reflected pressure with respect to the radius (a) of the target and the range (r) of the field point from the center of the target. Hickling also computed acoustic reflections from elastic spherical shells [5]. Empirical results on solid metal spheres in water were given by Hampton and McKinney [6], who demonstrated that the reflection from metal spheres immersed in water could not be

---

Manuscript submitted June 12, 1978.

described by purely geometric theory, and by Diercks [7], who demonstrated qualitative agreement between the computations of Hickling and measurements made in a lake. Precise quantitative comparisons between normal mode theory and experiment were first carried out by Neubauer et al. [8], who performed a series of precise steady-state measurements on solid metal spheres in a controlled acoustic tank facility. These measurements demonstrated quantitative agreement between computations, based on the normal mode series, and experiment, to within the known accuracy of the shear velocities of the materials used in the sphere fabrications. This work [8] covered the ka range $0 < ka \leqslant 30$. Dragonette et al. [9] demonstrated empirically that quantitative steady state results could be obtained from measurements made with short broadband incident acoustic pulses. This transient technique [9] will be described further in Chapter II. Comparisons between normal mode theory and experiment for elastic cylinders in water are more recent [10] but again demonstrated excellent agreement between the theory based on the infinite elastic cylinder and near-real-time experiments performed with finite length cylinders in a laboratory tank. The preceding theoretical and empirical papers [1-10] established that the normal mode series formulation of the acoustic reflection from elastic metal targets quantitatively describes measured results up to at least $ka = 30$, without the necessity of material absorption being included in the theory.

B. Circumferential Wave Theory and Empirical Observation

Empirical observations by Barnard and McKinney [11] at the Defense Research Laboratory (DRL) demonstrated periodic, multiple echo returns when solid and hollow brass cylinders ($ka \simeq 40$) were illuminated by short acoustic pulses. Subsequent empirical work and analysis at DRL by Diercks [12], Horton [13], and others [14,15] proposed the existence of two types of circumferential waves which were compared to flexural and longitudinal modes on infinite plates. The researchers at DRL recognized a similarity between the circumferential behavior of the waves they observed and the waves discussed by Franz [16] in his work on the diffraction of electromagnetic waves by conducting cylinders and spheres. The name given by Franz to these circumferential waves was translated "creeping waves". The original analogy between the acoustic waves observed at DRL and the purely geometrically diffracted circumferential waves considered by Franz broke down, because the speeds of the observed acoustic circumferential waves were from 33% to 300% higher than the speed of sound in the medium surrounding the targets, whereas analogy with the "creeping waves" of Franz would have predicted a speed slower than that in the surrounding medium.

Überall and collaborators at Catholic University also noted the similarity between the circumferential behavior of empirically observed acoustic waves and waves studied in electromagnetic theory. They began an in-depth theoretical program which employed a Watson [17] transformation in the description of both rigid and elastic scatterers. This technique had been used in the study of the propagation of radio waves around the earth [18] and, as mentioned previously, in the studies of the diffraction of electromagnetic waves by cylinders [16]. The Watson transformation offered certain advantages, namely, the opportunity to isolate the individual mechanisms responsible for the empirically observed circumferential waves and rapid convergence of the solution. This latter advantage was particularly significant, since the normal mode series was considered to be practical only at low ka, because of its slow convergence and the expense of computation. (Advances in computer technology make present high ka Rayleigh series computations both possible and economical [19].) The Catholic University group applied the Watson transformation to cylinders with rigid and soft boundary conditions and predicted the existence of true Franz type, or purely geometrically diffracted, circumferential waves [20]. Application of the Watson method to solid elastic cylinders [21] revealed two groups of poles corresponding to two types of circumferential waves. The Franz-type or geometrically diffracted waves were again observed, and, in addition, poles related to elastic circumferential waves, called R or Rayleigh-type waves, whose speed and properties depend primarily on the elastic constants of the target, were found. Grace and Goodman [22] also presented theoretical evidence for the existence of R-type waves.

Experimental detection of the acoustic Franz-type or purely geometrically diffracted wave was accomplished by Neubauer [23] and by Harbold and Steinberg [24]. The first experiments designed to demonstrate elastic R-type circumferential waves, that is, those related to R-type poles, were performed by Bunney et al. [25] and by Neubauer [26]. Both of these researchers [25,26] used short incident pulses and narrow beam sources to observe the scattering from solid aluminum cylinders. Their results demonstrated the existence of a train of periodic echoes with a circumferential speed close to the shear wave velocity in aluminum. Neubauer's [26] work included schlieren visualization of wavefronts resulting from the circumferentially traveling waves. These experiments gave mainly high *ka* results (*ka* values between 50 and 500). Originally the mechanism responsible for the periodic pulse trains observed [25,26] was, in fact, considered to be multiple circumnavigations of the cylinder by the Rayleigh wave (the R_1 pole of Ref. 21). Later work by Neubauer and Dragonette [27] showed that multiple internal reflections of shear waves could produce the observed effect, and this multiple reflection analysis was supported by the theoretical work of Brill and Überall [28], who demonstrated the circumferential behavior of the radiation from multiply internally reflected waves. Theoretical [29] and measured attenuation [30] of the Rayleigh wave on submerged flat surfaces also gave attenuations too large to support the conclusion that Rayleigh waves were the source of the multiple returns observed at high *ka* in Refs. 25 and 26. In this present work, a prediction of the *ka* range at which an R_1 circumferential wave can be significant and an empirical observations of the wave are accomplished.

C. Comparison of the two approaches and scope of the present work

The normal mode solutions give a straightforward method of obtaining the scattered acoustic pressure vs frequency, limited only by the expense involved in summing a slowly convergent series. Experimental results have been obtained which agree with the computation to a high degree of accuracy. The major disadvantage of this approach is that individual physical phenomena, such as surface waves, which make up the solution are not immediately obvious; however, techniques for isolating individual mechanisms are described in Chapter II and used throughout this work.

The Watson transformation of the normal mode series has the advantage that it isolates individual circumferential waves and the disadvantage that the poles must be found and interpreted and their significance judged.

The present work investigates the relationship between the normal mode solutions and the various propagation modes in cylinders, especially circumferential waves, which contribute to the steady state solution. A correspondence is demonstrated between the circumferential waves predicted by the Catholic University researchers and resonances in the normal mode series solutions. Families of resonances will be identified with the "creeping wave poles" discussed in Ref. 21. Based on this identification the R_1 or Rayleigh circumferential wave is

predicted to be of significance only in the region $ka < 20$, and the first experimental observation of backscattered circumferential radiation from this wave is demonstrated. Individual mechanisms are also isolated directly from the Rayleigh series formulation by the application of Fourier transform techniques which determine the response of the targets to transient signals. In this way hypotheses and conlusions concerning the amplitude, velocity, and attenuation of predicted phenomena are investigated. Calculations and comparisons of the total form function and the amplitudes of individual normal modes are made. These comparisons demonstrate that the reflection from solid metal cylinders is made up of a superposition of generally narrow resonant responses superimposed on a background attributable to reflection from a cylinder with rigid boundary conditions. This observation is formalized by applying the resonance formalism of nuclear reaction theory.

Circumferential waves on cylindrical shells are investigated by analysis of the calculated form function for elastic shells, by Fourier analysis of the transient response of a shell, and by comparison between the properties of the circumferential waves on cylindrical shells and the characteristics of Lamb waves on flat plates. Much new information concerning the properties and significance of these waves is obtained, and some misleading or erroneous information currently existing in the literature is corrected.

II. GENERAL THEORETICAL FOUNDATION

The Rayleigh series expression for the scattered acoustic pressure, $p_s(\theta)$, which results when a plane wave, $p_o e^{ikx}$, illuminates an infinite elastic cylinder, in the geometry described by Fig. 1, is given in many publications [3,10,21,31,32]. The following form is found in Refs. 31 and 32:

$$p_s(\theta) = -p_o \sum_{n=0}^{\infty} \epsilon_n (i)^n \left[\frac{J_n(Z)\, L_n - Z\, J_n'(Z)}{H_n(Z)\, L_n - Z\, H_n'(Z)}\right] H_n(kr) \cos n\theta. \tag{1}$$

The time dependence $e^{-i\omega t}$ is suppressed. In Eq. 1, ϵ_n is the Neumann factor ($\epsilon_n = 2$, $n = 0$; $\epsilon_n = 1$, $n > 0$), J_n is a Bessel function, H_n is a Hankel function of the first kind, $Z \equiv ka$, and the L_n are the quotients of two 2-by-2 matrices:

$$L_n = \frac{\rho}{\rho_s} \frac{D_n^{(1)}[Z]}{D_n^{(2)}[Z]} = \frac{\rho}{\rho_s} \frac{\begin{vmatrix} a_{11} & a_{13} \\ a_{21} & a_{23} \end{vmatrix}}{\begin{vmatrix} a_{11} & a_{13} \\ a_{31} & a_{33} \end{vmatrix}} \tag{1a}$$

where the matrix elements a_{ij} are given in Ref. 31. In the far field where $r > a$, $H_n(kr)$ may be written in its asymptotic form

$$H_n(kr) = \left|\frac{2}{\pi kr}\right|^{1/2} e^{ikr - in\pi/2 - i\pi/4} \tag{2}$$

and, defining

$$\left[\frac{J_n(Z)\, L_n - Z\, J_n'(Z)}{H_n(Z)\, L_n - Z\, H_n'(Z)}\right] = G_n(Z), \tag{3}$$

the far field pressure scattered by an infinite cylinder illuminated by a plane incident wave may be written

$$p_s(\theta) = -p_o\, e^{ikr} \left|\frac{2}{\pi kr}\right|^{1/2} e^{i\pi/4} \sum_{n=0}^{\infty} \epsilon_n G_n(Z) \cos(n\theta). \tag{4}$$

For backscattering, $\theta = \pi$ and

$$p_s(\pi) = -p_o\, e^{ikr} \left|\frac{2}{\pi kr}\right|^{1/2} e^{i\pi/4} \sum_{n=0}^{\infty} \epsilon_n (-1)^n\, G_n(Z). \tag{5}$$

A quantity called the far field form function, f_∞, is defined to give a nondimensional representation of the scattered pressure. In keeping with the definition used extensively in the literature [4,5,7-10,31,32]

$$f_\infty(\theta) = \left|\frac{2r}{a}\right|^{1/2} \frac{p_s(\theta)}{p_o}. \tag{6}$$

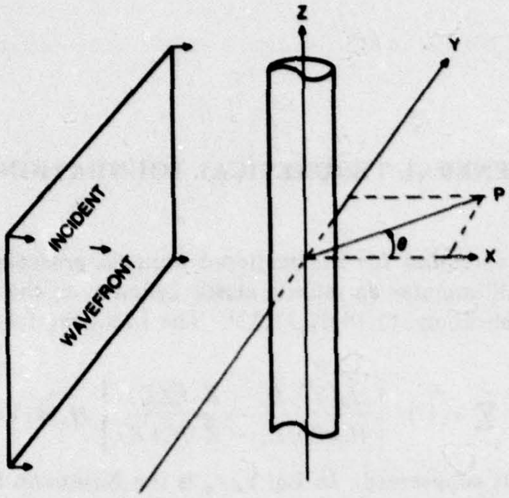

Fig. 1 – The geometry used in the description of the scattering of a plane wave by an infinitely long cylinder.

This definition is chosen since it results in $|f_\infty| = 1$ for the case of a purely rigid cylinder in the high frequency limit. From Eqs. 4 and 5 the expressions for $f_\infty(\theta)$ and $f_\infty(\pi)$ for an elastic cylinder are given by

$$f_\infty(\theta) = \frac{-2}{(i\pi Z)^{1/2}} \sum_{n=0}^{\infty} \epsilon_n \, G_n(Z) \cos(n\theta) \tag{7a}$$

and

$$f_\infty(\pi) = \frac{-2}{(i\pi Z)^{1/2}} \sum_{n=0}^{\infty} \epsilon_n (-1)^n \, G_n(Z). \tag{7b}$$

Using Eq. 7b, the individual normal modes or partial waves which make up the backscattered form function are defined as

$$f_n(\pi) = \frac{-2}{(i\pi Z)^{1/2}} \epsilon_n (-1)^n \, G_n(Z) \tag{7c}$$

where

$$f_\infty(\pi) \equiv \sum_{n=0}^{\infty} f_n(\pi). \tag{7d}$$

Computed plots of f_∞ vs ka, obtained from Eq. 7b are called reflection function plots, and such curves give a dimensionless representation of the scattered steady state pressure vs frequency. This representation can describe the scattering at any combination of radius and frequency within the ka limits of the calculation. Equations 7a and 7b give steady state values of f_∞, so that a continuous wave or very long pulse experiment can be used to obtain a direct comparison between experimental and calculated results [8]. Such an experimental method is tedious and excessively time consuming, as each experiment at each single frequency gives one point on the reflection function curve. To overcome this practical difficiency, methods to obtain the steady state quantity f_∞ from short broadband incident pulses were developed [9, 10].

If the incident sound wave in the geometry described by Fig. 1 is not steady state but a pulse, $p_i(\tau)$, with a Fourier transform $g_i(ka)$ given by

$$g_i(ka) = \int_{-\infty}^{\infty} p_i(\tau)\, e^{ika\tau}\, d\tau \tag{8}$$

then from Eqs. 6 and 8, the backscattered pressure has a Fourier transform $g_s(ka, \pi)$ given by

$$g_s(ka, \pi) = \left(\frac{a}{2r}\right)^{1/2} f_\infty(ka, \pi)\, g_i(ka) \tag{9}$$

and $|f_\infty(ka, \pi)|$ can be obtained from

$$|f_\infty(ka, \pi)| = \left(\frac{2r}{a}\right)^{1/2} \frac{|g_s(ka, \pi)|}{|g_i(ka)|}. \tag{10}$$

The quantity τ is a dimensionless time parameter

$$\tau = \frac{ct - r}{a} \tag{11}$$

which is normalized to be zero when the incident pulse is coincident with the position of the center of the cylinder. Equation 10 is the basis by which a steady state quantity $|f_\infty(ka, \pi)|$ can be obtained over a broad frequency range by a single short pulse experiment. The incident and reflected pulses are digitized, their transforms computed, and the division indicated in Eq. 10 carried out [9]. With present minicomputer technology this entire procedure can be accomplished in a near real time framework [10]. The experimental system used is discussed in Appendix B. The ka range over which f_∞ is obtained depends of course on the bandwidth of the incident pulse. Theoretical computations of the scattered echoes which result when a short incident pulse with a known spectrum, $|g_i(ka)|$, is used to insonify a target with a known $f_\infty(\theta, ka)$ can be obtained by using Eq. 9. This computation procedure allows the isolation of the individual mechanisms which contribute to the steady state scattered pressure. These pulse calculations are of significant value for many reasons, the most important of which is, that the theoretically formulated incident pulses used, can be made shorter than any which can be reasonably achieved in the laboratory. This allows isolation of closely spaced echoes which cannot be accomplished at a resonable cost in the laboratory. In addition theoretical computations can simulate experimental measurements over a large number of frequencies, target materials, target sizes, and target shell thickness that would be impossible to duplicate economically in a laboratory. In the theoretical procedure an incident pulse $p_i(\tau)$ with a known spectrum, $|g_i(ka)|$, is used to insonify a target whose form function can be computed. Computation of the form function and the procedure indicated in Eq. 9 are accomplished by the computer, and the scattered echo, $p_s(\tau)$, is described by

$$p_s(\tau) = 1/2\pi \int_{-\infty}^{\infty} g_s(ka)\, e^{-ika\tau}\, dka. \tag{12}$$

Solutions to Eq. 12 are obtained by using fast Fourier transform techniques in the computer.

III. THE RELATIONSHIP BETWEEN CREEPING WAVES AND THE NORMAL MODES OF VIBRATION OF A CYLINDER

A. The rigid cylinder

The acoustic reflection from a rigid cylinder has been well understood since the prediction [20] and empirical observation [23,24] of the Franz wave, and only a few ideas relating to the direct use of the form function curves to derive Franz wave properties can be added. In the case of a rigid cylinder, $G_n(Z)$ as defined in Eq. 3 reduces to

$$G_n^{(R)}(Z) = \frac{J_n'(Z)}{H_n'(Z)} \tag{13}$$

and the form function for a rigid cylinder is given by

$$f_\infty^{(R)}(Z) = \frac{-2}{(i\pi ka)^{1/2}} \sum_{n=0}^{\infty} \epsilon_n (-1)^n G_n^{(R)}(Z). \tag{14}$$

A plot of $f_\infty(\pi)$ vs ka computed from Eq. 14 is given in Fig. 2. Since by definition the boundary conditions imposed to obtain Fig. 2 preclude penetration into the cylinder, the backscattered reflection function curve can include contributions only from specular reflection and diffraction.

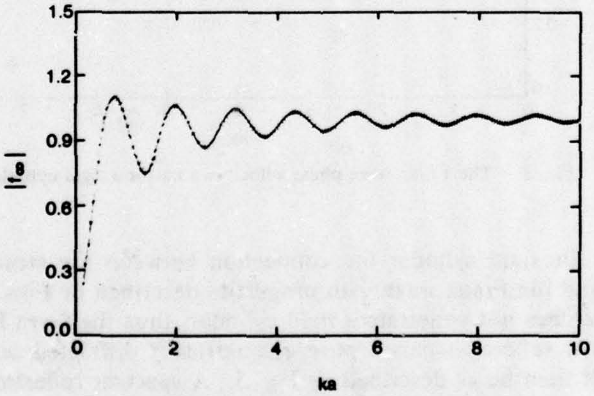

Fig. 2 – The form function for a rigid cylinder.

In the creeping wave solution Eq. 14 is transformed from an infinite series of n terms into a series of "creeping surface waves" by the Watson transformation [18,20]. The creeping waves arise as the residue of poles in the complex ν plane determined from the equation

$$H_\nu'(Z) = 0 \tag{15}$$

with solutions

$$\nu_l(\omega) = Z+(Z/6)^{1/3}e^{i\pi/3}\,q_l - \left[\frac{6}{Z}\right]^{1/3} e^{-i\pi/3}\left[\frac{1}{10q_l}+\frac{1}{180}+\frac{q_l^2}{180}\right] \tag{16}$$

where the q_l are the zeroes of the first derivates of the Airy function as defined by Franz [17]. The index $l = 1, 2, 3...$, and l increases in the direction of increasing real and imaginary parts of ν_l. The attenuation, α_l^f, of the l^{th} Franz wave in nepers/radian is given by

$$\alpha_l^f(\mathrm{Np/rad}) = \mathrm{Im}\ \nu_l \tag{17a}$$

and the phase velocity, c_p^F, is given by[20]

$$c_p^F/c = \frac{Z}{R_e\ \nu_l} \tag{17b}$$

where c is the velocity of sound in water. Calculations based on Eqs. 16 and 17a demonstrate that only the $l = 1$ or first Franz wave is of significant magnitude, and Figs. 3 and 4 give computations of the attenuation and phase velocity of this first Franz wave as a function of ka as computed from Eqs. 17b and 17a.

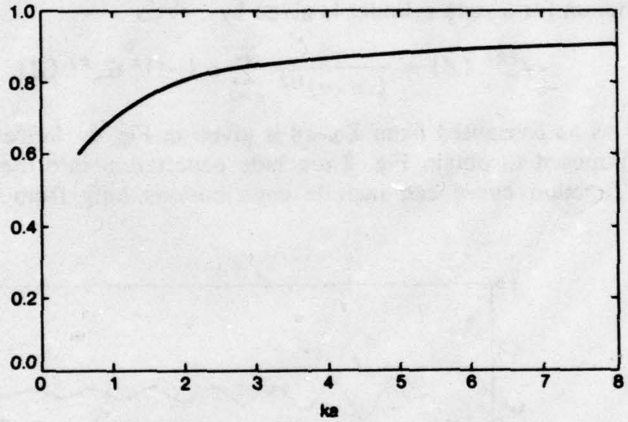

Fig. 3 – The Franz wave phase velocity vs ka for a rigid cylinder.

In the case of the rigid cylinder the connection between the steady state form function f_∞^R, given in Fig. 2 and the Franz wave with properties described by Figs. 3 and 4 is not difficult to determine. Sound does not penetrate a rigid cylinder, thus the form function must be made up entirely of specular reflection plus a pure geometrically diffracted contribution. The backscattered return must then be as described by Fig. 5. A specular reflection begins at point A of Fig. 5, and two Franz waves begin at points B and C and take the paths shown. This well understood result can, however, be taken further. The reflection function given in Fig. 2 is a steady state function, and the knowledge that this reflection function results from sound waves taking the circumferential paths shown in Fig. 5 leads to the following analysis. Because the two diffracted waves BC and CB take the same path and travel at the same speed, they are always in phase with each other in the backscattered direction. Computations based on Eqs. 16 and 17a demonstrate that for $ka > 1$ only these first Franz returns need be considered; that is, the contribution from succeeding circumnavigations of the cylinder are too small in amplitude

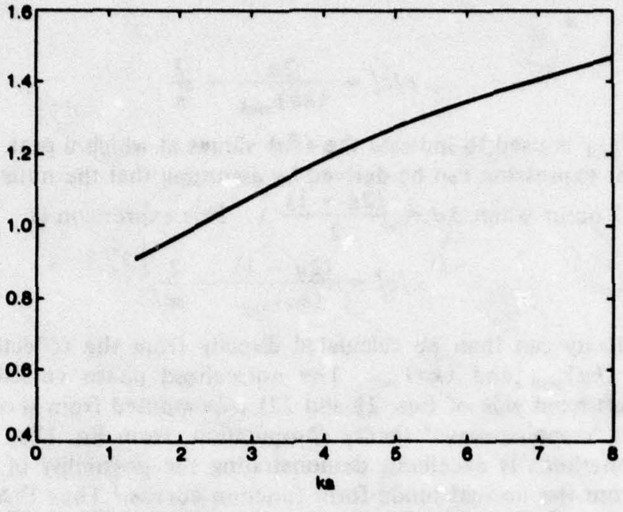

Fig. 4 – The Franz wave attenuation vs ka for a rigid cylinder.

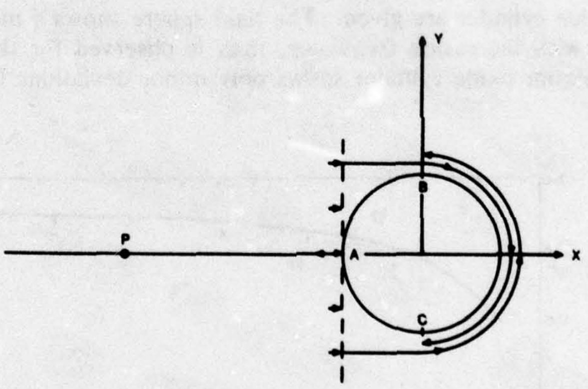

Fig. 5 – Source of backscattered echoes from a rigid cylinder.

to be significant. The difference in the time of arrival, at the field point P, between the specular and diffracted waves is

$$\Delta t = \frac{2a}{c} + \frac{\pi a}{c_p^F}. \tag{18}$$

The difference in path lengths traveled by the backscattered specular and Franz wave contributions at the field point P is expressed as

$$\Delta d = 2a + \frac{\pi a \ c}{c_p^F}. \tag{19}$$

If it is assumed that the peaks in the reflection function curve (Fig. 2) occur when the specular and Franz contributions add in phase at P, then peaks occur when

$$\Delta d = a(2 + \pi c/c_p^F) = n\lambda = \frac{n\ 2\pi}{k} \tag{20}$$

which leads to

$$c/c_p^F = \frac{2n}{(ka)_{peak}} - \frac{2}{\pi}. \tag{21}$$

The notation $(ka)_{peak}$ is used to indicate the (ka) values at which a peak in $|f_\infty^R|$ as seen in Fig. 2 occurs. A similar expression can be derived by assuming that the nulls in the reflection function curve of Fig. 2 occur when $\Delta d = \frac{(2n-1)}{2}\lambda$. This expression is

$$c/c_p^F = \frac{(2n-1)}{(ka)_{null}} - \frac{2}{\pi}. \tag{22}$$

A Franz wave velocity can than be calculated directly from the reflection function curve by determination of $(ka)_{peak}$ and $(ka)_{null}$. The normalized phase velocity c_p^F/c (which is the reciprocal of the left-hand side of Eqs. 21 and 22) is computed from these equations and compared to the direct "creeping wave" theory computation, from Eq. 17b, in Fig. 6. Agreement between the two methods is excellent, demonstrating the possibility of obtaining Franz wave velocity directly from the normal mode form function curves. Thus Franz wave velocities can be obtained for bodies for which no creeping wave analysis exists. Examples are given in Figs. 7 and 8, where computed form functions and derived Franz wave velocities for a rigid sphere and an aluminum oxide cylinder are given. The rigid sphere shows a much more rapid rise in Franz wave velocity with increasing frequency, than is observed for the rigid cylinder. The velocity for the aluminum oxide cylinder shows only minor deviations from the rigid cylinder curve.

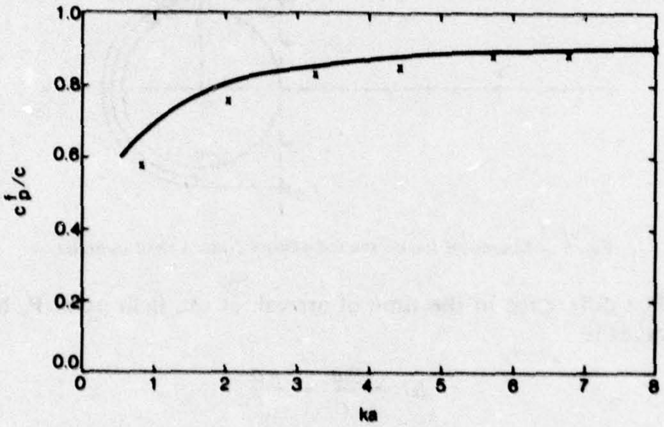

Fig. 6 – A comparison between the computed Franz velocity for a rigid cylinder (–) and values estimated from the form function curve (x).

The attenuation of the Franz wave as a function of *ka* can also be investigated directly from the normal mode calculation. Here the reduction in amplitude of the successive oscillations is assumed due to the increase in attentuation of the Franz wave as a function of *ka*. The reduction in magnitude of the oscillations in Fig. 2 with increasing *ka* should then give a measure of the Franz wave attenuation vs *ka*. A comparison of attenuation values obtained from creeping wave theory for a rigid cylinder and values obtained from the form function curve is

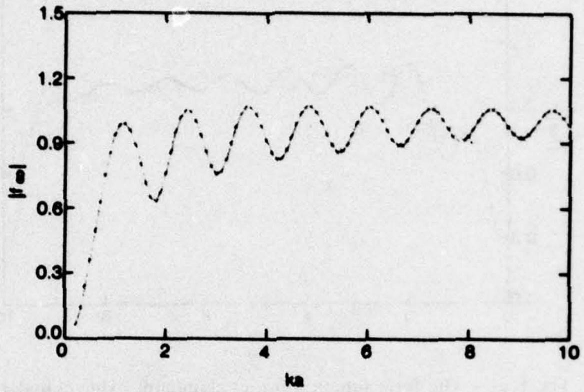

Fig. 7(a) – The form function vs ka for a rigid sphere.

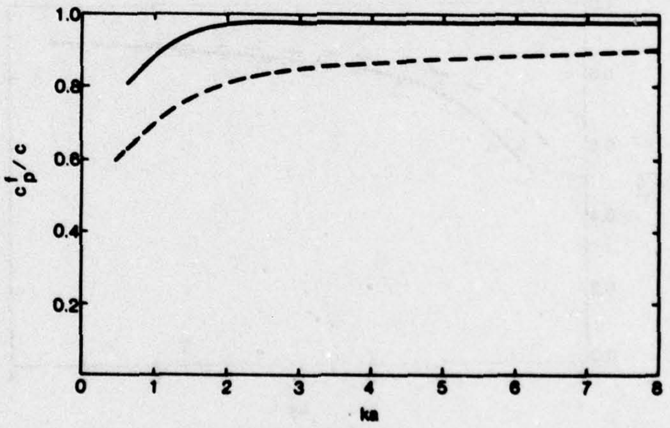

Fig. 7(b) – Franz wave velocity estimated from (7a) for a rigid sphere (——) and Franz wave velocity for a rigid cylinder (- - -).

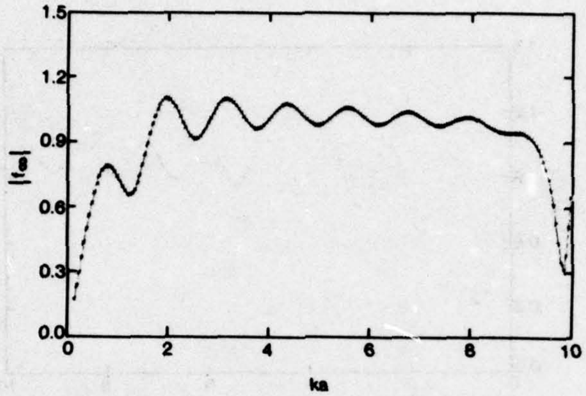

Fig. 8(a) – The form function for an aluminum oxide cylinder.

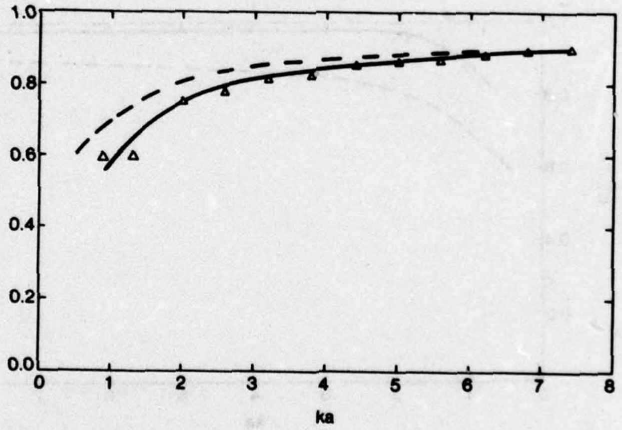

Fig. 8(b) – Franz wave velocity estimated from the form function (——) and Franz wave velocity for a rigid cylinder (- - -).

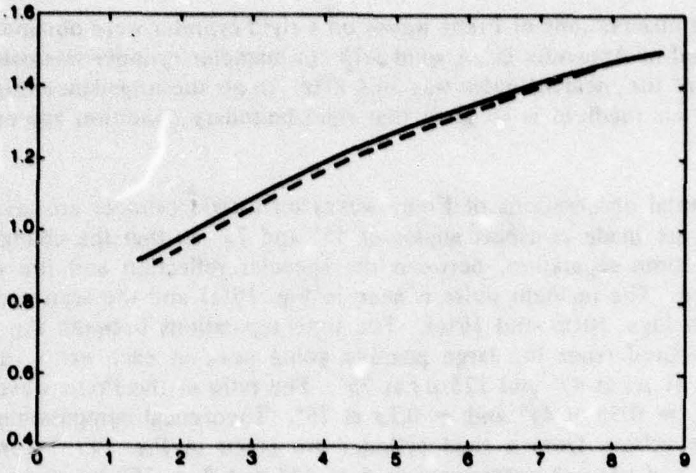

Fig. 9(a) – Franz wave attenuation for a rigid cylinder obtained directly (——) and estimates obtained from the form function curve (- - -).

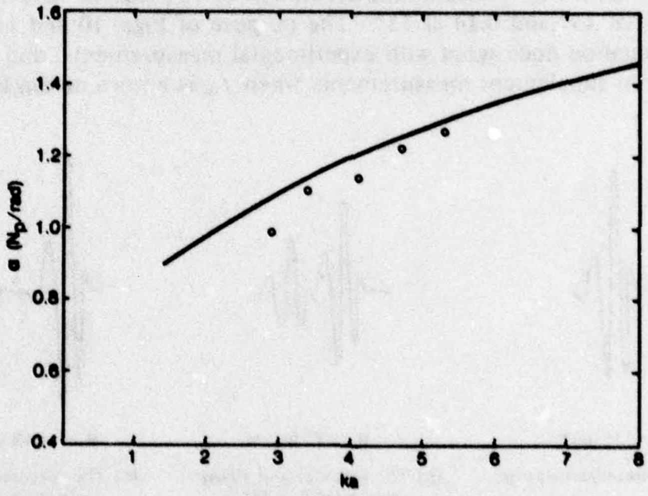

Fig. 9(b) – Franz attenuation estimates for an aluminum oxide cylinder (o) compared to the rigid cylinder (——).

given in Fig. 9a. In Fig. 9b the attenuation is given for an aluminum oxide cylinder for which no direct creeping wave data are available. The rigid cylinder curve is included in Fig. 9b, for comparison.

Empirical observations of Franz waves on a rigid cylinder were obtained in the acoustic air facility described in Appendix B. A solid 3.18 cm diameter cylinder was used as the target, and the frequency of the incident pulse was 34.4 kHz. In air the impedance mismatch between the aluminum and air medium is so great that rigid boundary condition assumptions are successfully achieved.

Experimental observations of Franz waves on a rigid cylinder are given in Fig. 10. The measurements are made at aspect angles of 45° and 75° so that the changes, both in relative amplitude and time separation, between the specular reflection and the Franz wave can be clearly observed. The incident pulse is seen in Fig. 10(a) and the scattered echoes at 45° and 75° are seen in Figs. 10(b) and 10(c). The time separations between the specular and Franz waves are measured from the large positive going peak in each echo. The measured time differences are 81 μs at 45° and 125 μs at 75°. The ratio of the Franz wave to specular amplitude is $p_F/p_{\text{spec}} = 0.56$ at 45° and $= 0.13$ at 75°. Theoretical computations, based on Eqs. 9 and 12, of the echoes from a rigid cylinder are given in Fig. 11. Figure 11(a) shows the incident pulse, and the echo responses at $\theta = 45°$ and $\theta = 75°$ are given in Figs. 11(b) and 11(c) respectively. The center dimensionless frequency of the pulse is $k_o a = 10$. The computations were made using Eqs. 9 and 12 as discussed in Chapter II. The theoretical computations agree closely with experiments in the relative magnitudes and positions of the Franz waves. The values obtained from Fig. 11 are a time separation of 78 μs at 45° and 125 μs at 75°, and a ratio p_F/p_{sec} of 0.57 at 45° and 0.14 at 75°. The purpose of Figs. 10 and 11 is to demonstrate that the echo computation does agree with experimental measurements, and can be used to isolate mechanisms or to supplement measurements when f_∞ is known or can be computed.

(a) The incident pulse, (b) The specular and Franz echoes at $\theta = 45°$, (c) The specular and Franz echoes at $\theta = 75°$,

Fig. 10 – The experimental observation of the Franz wave radiation from a rigid cylinder.

B. The elastic cylinder problem

In contrast to the essentially well understood rigid cylinder problem, the relationship between the normal mode and creeping wave solutions to the elastic cylinder problem were unknown before this work began. That relationship is established in this work, and as a result,

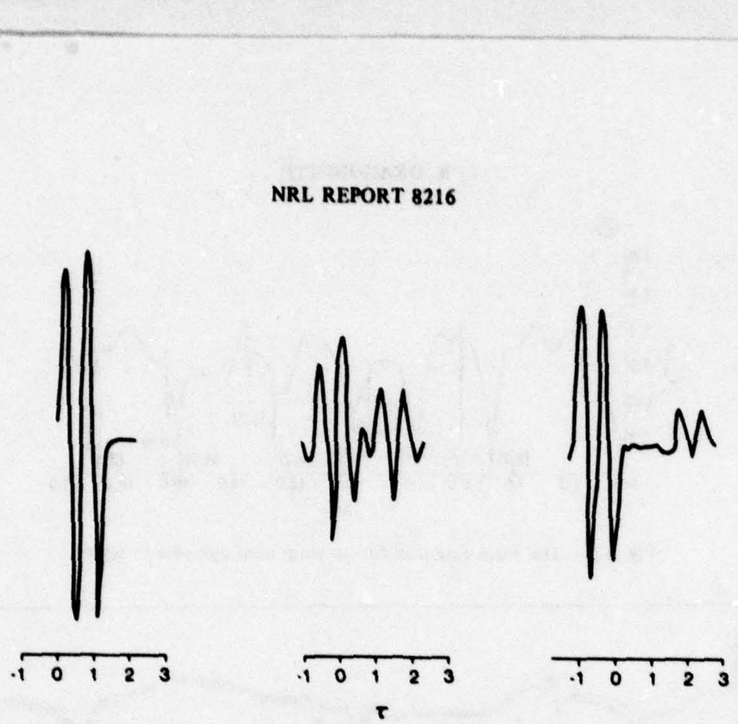

(a) The incident pulse.

(b) The specular and Franz echoes at $\theta = 45°$.

(c) The specular and Franz echoes at $\theta = 75°$

Fig. 11 – Computation of the scattering of a two cycle incident pulse by a rigid cylinder.

resonances in the normal mode solution can be identified with specific R-type circumferential waves predicted by creeping wave theory. The *ka* range over which one such wave, the R_1 or Rayleigh wave makes a significant backscattering contribution has been the subject of much conjecture [25-28,33] in the literature. The results obtained here indicate a limited, low *ka*, region of importance of the R_1 circumferential wave in contrast to previous hypotheses [25,26,33], and the first experimental observation of backscattered circumferential radiation from the true Rayleigh wave was accomplished in the low *ka* region where it is predicted. Computation and analysis of the effects of the normal mode resonances on the backscattered $|f_\infty|$ demonstrate further that the form function is made up of a rigid background on which narrow resonances are superimposed. A formalism reflecting the above result is developed based on an approach suggested by Dr. L. Flax and Dr. H. Überall which makes use of the methods of nuclear reaction theory.

C. Elastic cylinder results

The backscattered form function for an elastic aluminum cylinder in water is calculated from Eq. 7b and given in Fig. 12 over the range from $0.2 \leqslant ka \leqslant 20$. The curve is calculated in *ka* steps of $\Delta ka = 0.01$. A comparison between this theoretical computation and an experiment using the short pulse experimental technique described in Chapter II is given in Fig. 13. In Fig. 13 the theoretical curve is computed in intervals of $\Delta ka = 0.05$ which is compatible with the Δka isolation that can be achieved experimentally. Agreement between theory and experiment is within 2%. The form function curve seen in Fig. 12, shows that over the range $0.2 \leqslant ka \leqslant 4.7$ the aluminum reflection curve is very similar to that of the rigid cylinder (Fig. 2). This region of similarity is followed by marked irregular oscillations and these oscillations continue as $ka \rightarrow \infty$, if no absorption is included in the theory. Damping of the oscillations as *ka* increases will occur when absorption becomes significant [34], but for metals such as aluminum, experimental results indicate [8-10] that absorption need not be included over the ranges of *ka* that will be considered here.

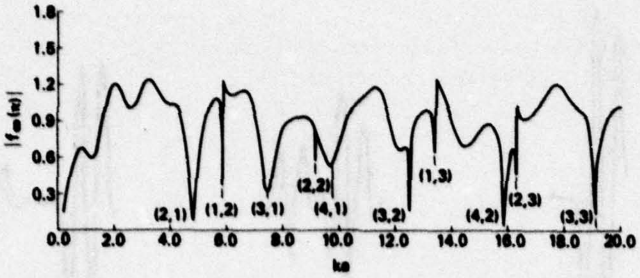

Fig. 12 – The form function for an aluminum cylinder in water.

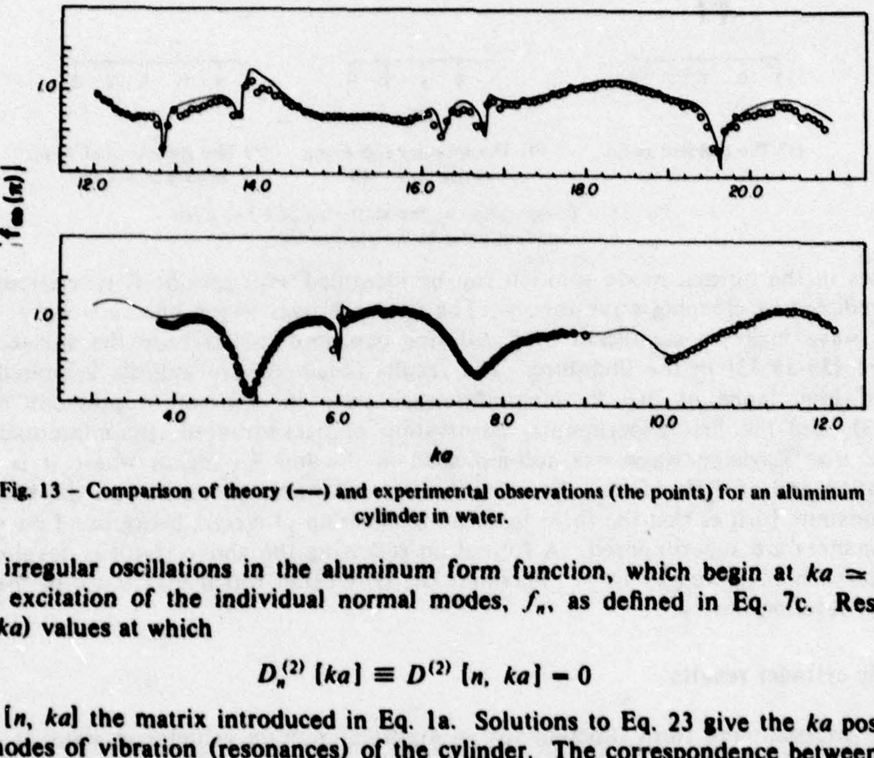

Fig. 13 – Comparison of theory (——) and experimental observations (the points) for an aluminum cylinder in water.

The irregular oscillations in the aluminum form function, which begin at $ka \simeq 4.5$, are related to excitation of the individual normal modes, f_n, as defined in Eq. 7c. Resonances occur at (ka) values at which

$$D_n^{(2)}\,[ka] \equiv D^{(2)}\,[n,\, ka] = 0 \tag{23}$$

with $D_n^{(2)}\,[n,\, ka]$ the matrix introduced in Eq. 1a. Solutions to Eq. 23 give the ka position of the free modes of vibration (resonances) of the cylinder. The correspondence between the ka values at which irregularities in the form function occur and the ka values at which resonances occur is indicated in Fig. 12, where the resonances are identified by the subscript $(n,\, l)$. Here n is the mode number and l is the eigenfrequency, for example $(n,\, 1)$ means the fundamental resonance of the nth normal mode, $(n,\, 2)$ the first harmonic, etc. The "creeping wave" solution to the problem of the scattering of an incident plane wave by a solid aluminum cylinder was carried out by Doolittle et al. [21], who transformed Eq. 7b using the Watson technique. Doolittle found poles in the complex ν plane at the positions

$$D^{(2)}\,[\nu,\, ka] = 0. \tag{24}$$

He computed a series of R type, or elasticity related, poles and gave a table of the positions of the first six R type poles in the complex ν plane as a function of ka. Each pole gives rise to a circumferentialy traveling wave [21]. The relationship between Eqs. 23 and 24 form the basis for the correspondence between normal mode resonances and the individual circumferential waves predicted by the creeping wave theory. To obtain this relationship, it is necessary to consider the properties of the normal modes individually. Equation 7c describes the nth normal mode. The $n = 0$ term is the breathing mode, $n = 1$ the dipole term, $n = 2$ the quadropole, etc. The individual motions can be represented by a pair of standing waves $e^{i\pm(n\theta-\omega t)}$ traveling in the opposite directions with phase velocites

$$c_n(ka) = \frac{kac}{n} \tag{25}$$

and group velocities

$$c_n^g(ka) = c\,\frac{d(ka)}{dn}. \tag{26}$$

At a resonance of the nth mode exactly n wavelengths fit over the circumference of the body, and the lth eigenfrequency of the nth mode, $(ka)_{n,l}$ is the lth solution to Eq. (23). A comparison of Eqs. (23) and (24) leads to the connection between the creeping wave solution and the

$$\nu = \nu_l(ka) \tag{27}$$

related to R type circumferential waves with phase velocities

$$c_l(ka) = \left[\frac{kac}{\mathrm{Re}\,\nu_l}\right] \tag{28}$$

and group velocities

$$c_l^g(ka) = \frac{c}{d\mathrm{Re}\,\nu_l/dka}. \tag{29}$$

If now Re $\nu_l ka = n$, Eqs. 23 and 24 become identical in form and the modal velocities (Eqs. 25, 26) are identical to the creeping wave velocities (Eqs. 28, 29). Thus, when Re $\nu_l = n$, the lth Rayleigh type circumferential wave coincides with the wave speed, $c_n(ka)$, of the nth modal vibration. This hypothesis is demonstrated below. Table I gives the modal eigenfrequencies obtained from Eq. 23, and identified in Fig. 12, and the corresponding modal phase velocities are computed from Eq. 25. The breathing modes $(0, l)$ are not strongly excited, as evidenced from Fig. 12, but are included in Table I. The (1, 1) mode is generated in the region where the Franz wave or rigid reflection predominates and is also not observed in Fig. 12. The ka values at which Re $\nu_l\ (ka) = n$, are extrapolated from the work of Doolittle et al (Table II of Ref. 21), and comparisons are made between these extrapolated values and the normal mode resonances identified in Fig. 12. This comparison is shown in Table II, which also gives the computed values of the creeping wave phase velocity [21]. Tables I and II demonstrate that the ka values at which resonances occur correspond to ka values at which Re $\nu_l\ (ka) = n$. They demonstrate further the equality of the modal and circumferential wave velocities $c_n\ (ka)$ and $c_l(ka)$. The relationship is thus established between the (n, l) normal modes and the elastic or R type poles found by the "creeping wave" theory. The (n, l) normal mode resonances correspond to the R_1 creeping wave. For $n = 2$ (i.e., the (2,1) mode), the circumference of the cylinder is 2 wavelengths of the R_1 type wave, at the (3, 1) resonance, the circumference of the cylinder is exactly 3 wavelengths, etc. The R_2 circumferential wave is similarly related to the $(n, 2)$ normal mode resonances, and so on, with the (n, l) normal mode resonances related to the lth order Rayleigh or R_l Rayleigh type circumferential wave.

Table I
Modal eignvalues $(ka)_{nl}$ and mode speeds c_n/c for an aluminum cylinder in water

l / n	(ka_{nl})			c_n/c		
	1	2	3	1	2	3
0	–	–	9.43	–	–	∞
1	–	5.87	13.44	–	5.87	13.44
2	4.78	9.17	16.31	2.39	4.59	8.16
3	7.38	12.53	19.12	2.46	4.18	6.37
4	9.65	15.84	–	2.41	3.96	–
5	11.78	19.02	–	2.36	3.80	–

Table II
The correspondence between the normal mode resonances and the ka values at which $\mathrm{Re}\,\nu_l = n$. The target is and elastic aluminum cylinder in water.

Normal mode resonances			(ka) values at which $\mathrm{Re}\,\nu_1 = n$ from the Sommerfeld-Watson formulation of Ref. 21		Phase velocities c_l/c of the R_L circumferential wave when $\mathrm{Re}\,\nu_l = n$				
N	l	$(ka)_{nl}$	L	$(ka)_{nl}$	R_1	R_2	R_3	R_4	R_5
0	3	09.43	3	09.40	–	–	∞	–	–
	4	10.46	4	10.40	–	–	–	∞	–
	5	17.14	5	17.08	–	–	–	–	∞
1	2	05.87	2	05.80	5.85	–	–	–	–
	3	13.44	3	13.39	–	13.24	–	–	–
	4	16.02	4	15.90	–	–	16.04	–	–
2	1	04.78	1	04.85	2.37	–	–	–	–
	2	09.17	2	09.10	–	04.58	–	–	–
	3	16.31	3	16.28	–	–	08.16	–	–
3	1	07.38	1	07.30	2.45	–	–	–	–
	2	12.53	2	12.47	–	04.15	–	–	–
	3	19.12	3	19.05	–	–	06.36	–	–
4	1	09.65	1	09.70	2.40	–	–	–	–
	2	15.84	2	15.80	–	03.94	–	–	–
5	1	11.78	1	11.80	2.35	–	–	–	–
	2	19.02	2	18.90	–	03.79	–	–	–

The R_1 circumferential wave is related to the leaky Rayleigh wave [35] on a flat surface. This is the surface wave which, as ka increases, approaches the phase velocity of the Rayleigh wave on a flat infinite half space. The higher order R type waves are called "whispering gallery" waves and become lateral waves in the limit as $ka \to \infty$ [35]. Since the R_1 or Rayleigh wave is related to the $(n, 1)$ resonances in the normal mode solution, the influence of the circumferentially traveling Rayleigh wave on the backscattering from an aluminum cylinder can be inferred from the relative influence of the $(n, 1)$ modes on the form function seen in Fig. 12. The (2, 1), (3, 1), and (4, 1) resonances are observed to have a marked effect on the form function in the ka range from $4 \leqslant ka \leqslant 10$. For $n > 4$ the effects of the $(n, 1)$ resonances on $|f_\infty|$ are small, and in fact for $ka > 20$ no $(n, 1)$ modes were observed to influence $|f_\infty|$. The result of the calculations plotted in Fig. 12 and calculations of $|f_\infty|$ carried out between $20 \leqslant ka \leqslant 40$ (not shown) strongly indicate that the Rayleigh wave will not contribute significantly to the observed backscattering from an aluminim cylinder at ka values above $ka = 20$. This is a significant point, since the possibility of Rayleigh wave generation at high (ka) has been a matter of dispute in the literature [25-28,33]. This point will be explored in more detail below. Fig. 12 does show, however, that the (2,1), (3,1), and (4,1) resonances are major features of the form function curve for $ka < 10$. Nulls in the form function at the ka positions of these three resonances should be related to the interference between specular reflection and the circumferentially traveling Rayleigh wave. Specular reflection and Rayleigh wave radiation are known to be 180° out of phase in the flat surface case [30,36,37]. Verification of the above explanation of the nulls at the (2,1), (3,1), and (4,1) resonance values should be possible both by computing the low ka echo response of an aluminum cylinder to an incident short acoustic pulse and by experimentally determining the echo response of an aluminum cylinder at low ka. Both measurement and computation were done, and this experimental observation of the backscattered reradiation from a circumferentialy traveling Rayleigh wave was the first observation of this phenomenon.

The major difficulty in achieving an experimental observation of the Rayleigh wave at low ka is in obtaining a practical and possible combination of cylinder radius, frequency, and pulse length that allows the Rayleigh wave to be separated from the specular reflection. The best available combinations were an aluminum cylinder of radius $a = 0.635$ cm measured with a short pulse centered at frequencies $f_o = 386$ kHz and $f_o = 500$ kHz. Commercially available lead zirconate titinate transducers, with active elements 1.905 cm square were driven with a rectangular pulse, and the achieved pulse length was 5 cycles.

Both the small acoustic pool facility in which the measurements were carried out and the means by which the return echoes were digitized and displayed are discussed in Appendix B. Figure 14 shows the backscattering from the 0.625 cm radius aluminum cylinder at $f_o = 500$ kHz, or $k_o a = 13.5$. The backscattered echo consists of a specular return followed by a Rayleigh circumferential wave which is 180° out of phase with the specular return. The digitized display in Fig. 14 was plotted by the Versatek plotter. Even at this relatively low ka value the second traversal of the cylinder by the Rayleigh wave is already almost entirely in the noise 25 dB below specular reflection. The experimental result at $f_o = 386$ kHz, $(k_o a) = 10.4$ is given in Fig. 15. Here there is a slight overlap of the final cycle of the specular reflection and the first cycle of the Rayleigh wave, but the 180° phase shift can still be observed. At this ka, direct measurement can be obtained of the group velocity and attenuation, as the second transversal of the Rayleigh wave is now visible. The path difference between the first and second manifestations of the Rayleigh wave is $\Delta d = 2\pi a$. The measured group velocity is $c_R^g/c = 1.9$, in comparison to the estimated value of $c_R^g/c = 2.0$ obtained from Ref. 21. It is expected that the

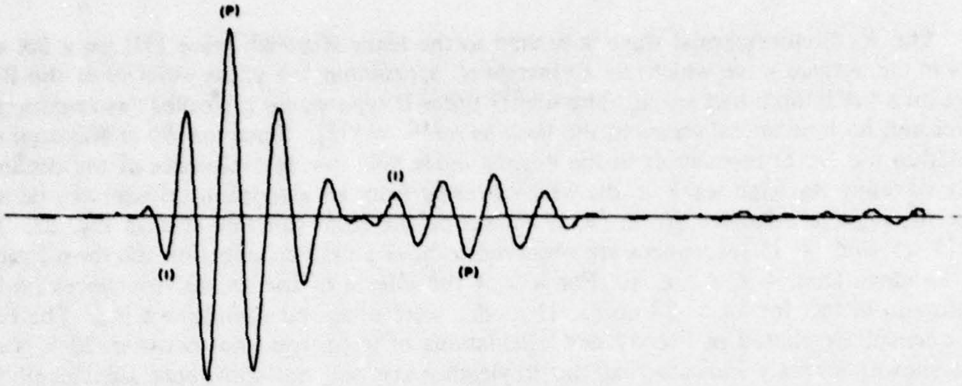

Fig. 14 – Experimental observation of the Rayleigh circumferential wave on an aluminum cylinder at $k_0a = 13.5$.

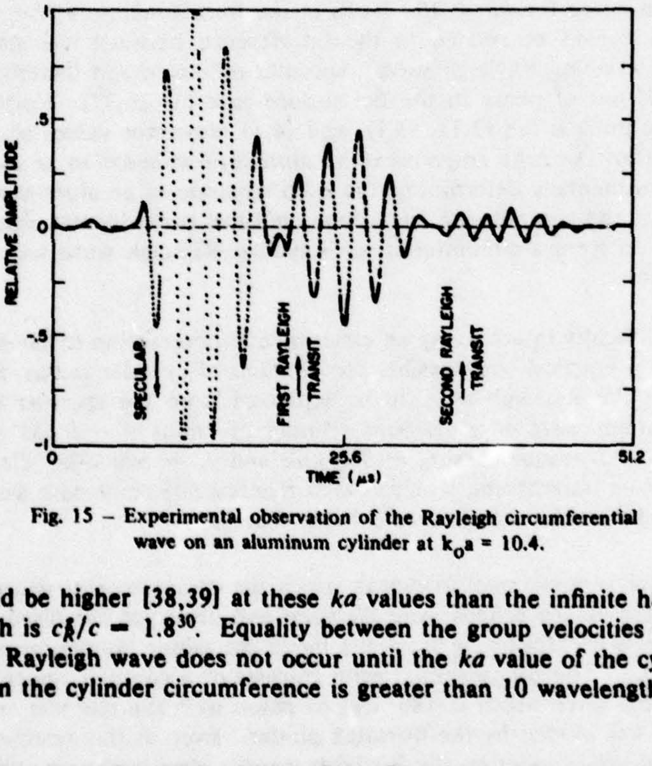

Fig. 15 – Experimental observation of the Rayleigh circumferential wave on an aluminum cylinder at $k_0a = 10.4$.

group velocity would be higher [38,39] at these *ka* values than the infinite half space Rayleigh wave velocity, which is $c_R^g/c = 1.8^{30}$. Equality between the group velocities of the flat surface and circumferential Rayleigh wave does not occur until the *ka* value of the cylinder reaches at least $ka \simeq 30$, when the cylinder circumference is greater than 10 wavelengths of the Rayleigh wave [38].

The fact that the circumferential velocity of the R_1 wave is a function of frequency, or *ka*, means that changes in the pulse shape should occur between the specular reflection and the R_1 circumferential wave. The velocity of sound in water is not a dispersive quantity, i.e. not a function of frequency, and the specular reflection has the same pulse shape as the incident wave. The Rayleigh velocity is a function of frequency over the range $0 \leqslant ka \simeq 30$ and thus is not constant over the range of frequencies represented by the incident pulse. Changes in pulse shape between the Rayleigh wave and the incident and specularly reflected waves are expected. In addition, Figs. 14 and 15 are digital representations of the recovered signal taken at intervals of 0.02 μs, or at about 100 points per cycle of the received pulse. No two digital representations are exactly alike, but with so many points having been taken, the only differences that are noticeable occur in the flattening effects at some of the peaks and valleys. In amplitude measurements these effects are negated by averaging many measurements. The phase shift of 180° was determined by comparing the pulse cycles labeled (1) and (P) in Fig. 14. Despite the slight change in pulse shape as discussed above, the beginning of the pulse labeled (1) and the characteristically large amplitude at the center of the pulse labeled (P) are present in both the specular and Rayleigh echoes and are 180° out of phase for these two echoes. The attenuation of the circumferential Rayleigh wave at $ka = 10.4$ is measured from Fig. 15 to be $|_R = 1.69$ Np/revolution where one revolution equals a travel path of one circumference. Computations of the response of an aluminum cylinder to an incident pulse should allow examination of the Rayleigh circumferential wave properties at even lower ka values than $k_o a = 10.4$ (the experimental conditions for Fig. 15). A one-cycle pulse can be programed as the incident pulse even though it is not readily attainable in a laboratory with normally available transducers. The computation of the reflection of a single-cycle pulse centered at $k_o a = 8.8$ is given in Fig. 16. Again specular and Rayleigh wave echoes are 180° out of phase. The group velocity obtained from Fig. 16 is $c_R^g/c = 2.4$, which compares to $c_R^g/c = 2.3$ estimated from Ref. 21.

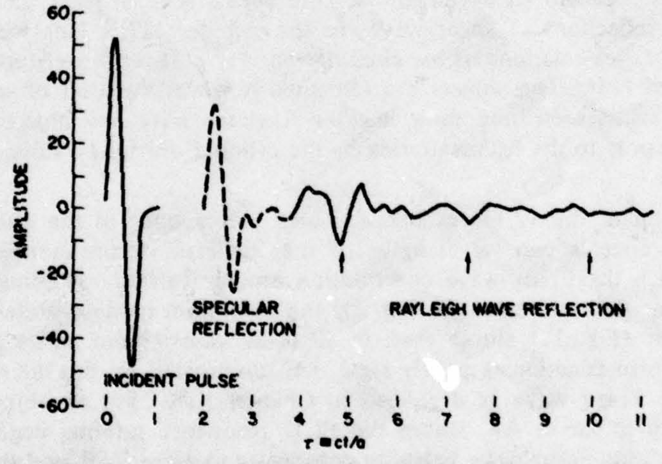

Fig. 16 – Computation of the echoes scattered by an aluminum cylinder at $k_o a = 8.8$.

Estimates of the expected Rayleigh wave attenuation due to radiation into the water can be made from the flat surface formula given by Dransfeld [29]:

$$\alpha_R = \frac{\rho c}{\rho_s c_r \lambda_R}. \tag{30}$$

The nonsubscripted variables refer to water, and the subscript R refers to the Rayleigh wave. Just as the limiting velocity is not achieved until $ka > 30$ for aluminum, it is not expected that computations made from Eq. 30 be exact for low ka. For aluminum the flat surface values for the variables in Eq. 30 are

$$\rho/\rho_s = 0.37;\ c/c_r = 0.55,\ \text{and}\ \lambda_R = 1.8\lambda$$

yielding

$$\alpha_R = \frac{0.113}{\lambda} = \frac{0.113k}{2\pi}\ cm^{-1} \tag{31a}$$

or

$$(2\pi a)\ \alpha_R \equiv \alpha_R = (0.113)\ (ka) \tag{31b}$$

where α_R is dimensionless.

Equation 31b gives $\alpha_R = 1.0$ at $ka = 8.8$ in comparison with the value $\alpha_R = 1.0$ obtained from Fig. 16. At $ka = 10.4$, Eq. 31b gives $\alpha_R = 1.2$ compared with $\alpha_R = 1.7$ obtained from the measurement in Fig. 15. The results indicate that a reasonable estimate of α_R can be made using the flat surface attenuation formula, even at low *ka*. The empirical observations given in Figs. 14 and 15 are the first observations of the true Rayleigh circumferential wave. Previous observations of circumferential waves on solid elastic cylinders have been made at *ka* values in the range $40 \leqslant ka \leqslant 400$ [25,26]. This high *ka* range was chosen because of the ease of pulse separation of any circumferential effects and, also, because Rayleigh-like circumferential wave properties would have more closely approximated the flat surface Rayleigh wave at high *ka*. The circumferential waves that were observed on aluminum were identified as Rayleigh [25] or "Rayleigh type" [26] waves. Further analysis of high *ka* circumferential results lead to an explanation of the effects seen in Refs. 25 and 26 in terms of multiple internal reflections of shear waves in the cylinder [27]. This view was further supported by theoretical calculations of the circumferentially radiated wavefronts which result from internal reflections [28]. The subject has remained however a matter of some conjecture [25-28,33], but the results seen here show that the Rayleigh wave has large enough amplitude to contribute significantly to the backscattering by the cylinder only at *ka* values below 20.

The excitation of the (2,1) resonance, which corresponds to the *ka* value at which the cylinder circumference is two wavelengths of the Rayleigh circumferential wave, marks the highest *ka* at which the Franz wave contribution can be isolated. A comparison of the form function curves for the rigid cylinder (Fig. 2), the aluminum oxide cylinder (Fig. 8a), and the aluminum cylinder (Fig. 12) shows that, in all these cases, there exists a region where the behavior of the form function is purely rigid, i.e., dominated by the interference of specular reflection and the Franz wave as described in Chapter IIIA. For an aluminum cylinder this behavior exists up to $ka \simeq 4.5$, where the (2,1) resonance minima begins. For aluminum oxide the specular plus Franz wave behavior persists up to $ka \simeq 9.90$, and the resonance null at $ka = 9.90$ in Fig. 8a is the (2,1) mode for aluminum oxide. Similar curves were computed for copper, brass, and tungsten carbide, and in all cases the generation of the (2,1) mode marks the end of the purely rigid behavior. The *ka* value at which the purely rigid behavior will end for a cylinder of a given material can be inferred by using aluminum as a reference. The (2,1) mode will be excited at

$$Z_{2,1}(\text{material}) = Z_{2,1}(Al) \cdot \frac{c_R(\text{material})}{c_R(\text{aluminum})}. \tag{31c}$$

The Rayleigh velocities used in Eq. 31c are flat surface numbers, and the equation assumes that the effect of curvature is the same for all materials, i.e., that the flat surface limit is reached when the circumference is greater than 10 Rayleigh wavelengths. Using the simple formula given in Eq. 31c, the *ka* position of the (2,1) resonance was predicted to within 1% for the materials discussed above.

IV. DEMONSTRATION THAT THE SCATTERING FROM SOLID ELASTIC CYLINDERS CAN BE SEPARATED INTO RIGID BACKGROUND AND RESONANCE PORTIONS

A. Preface

Junger and Feit [40] qualitatively considered the resonance features of the acoustic scattering by elastic bodies. They showed that resonances should appear where the sum of the mechanical and radiation impedance goes to zero. In part B of this chapter it is demonstrated that the acoustic scattering from a submerged aluminum cylinder can be described in terms of a rigid background term, with a resonance contribution superimposed on that background. The observed phenomenon is formalized in part C using the methods of nuclear scattering theory, so that mathematically explicit forms for the resonances and background, as well as expressions for the resonance widths, are obtained. It is necessary to establish the nature of the background before the formalism is developed because a parallel formalism could have been developed, using a soft or an intermediate background, which would have had no physical significance for the problem of the solid metal cylinder. The conclusions and formalism developed for the scattering from an aluminum cylinder apply to the scattering from any submerged solid cylinder whose density is greater then that of the surrounding fluid and whose shear and compressional sound speeds are greater than the speed of sound in the fluid.

B. Results

The results described in Chapter III demonstrated that the irregular characteristics of the form function for solid elastic cylinders are related to the normal modes of free vibration of the body, and these resonances often occur over a narrow frequency range as was seen in Fig. 12. It will be demonstrated in Figs. 17 through 20 that the resonances are superimposed on a background of reflection resulting from rigid boundary conditions, so that the elastic body can be regarded as a rigid body except in the frequency interval over which the resonances occur. In Fig. 17, the individual partial waves, $|f_n|$, from $n = 0$ through $n = 5$ are plotted vs ka for an aluminum cylinder. The f_n are described by Eq. 7c. The curves in Fig. 17 show that the amplitude of the individual partial waves $|f_n|$ have distinctive behavior in regions where the resonances occur. The eigenvalues l, are labeled along the curve in Fig. 17. The individual partial waves for both the infinitely rigid and the infinitely soft cylinder have no resonance irregularities, as seen in Fig. 18(a) and 18(b) respectively. The demonstration that the individual partial waves for a metal elastic cylinder consist of resonances superimposed on a rigid background is seen in Fig. 19. Here the $|f_2|$ and $|f_3|$ individual partial waves for rigid, soft, and elastic boundary conditions are plotted. It is clearly observed in Fig. 19 that the rigid and elastic curves are the same except in the region where resonances occur. The resonances for $l \geqslant 2$ are narrow resonances; the $l = 1$ eigenvalue which corresponds to the R_1 or Rayleigh surface wave is a broader resonance. A more dramatic example of the relationship between the elastic and the rigid solutions for a solid cylinder is seen in Fig. 20. Here the quantity $|f_2(\pi)^{\text{elastic}} - f_2(\pi)^{\text{rigid}}|$ is plotted vs ka, and the (2,1), (2,2), and (2,3) resonances are clearly isolated. As was noted, the (2,1) resonance and in fact the $(n, 1)$ resonances in general are broader than the narrow resonances which occur for higher order eigenfrequencies, i.e. $l > 1$. A method of

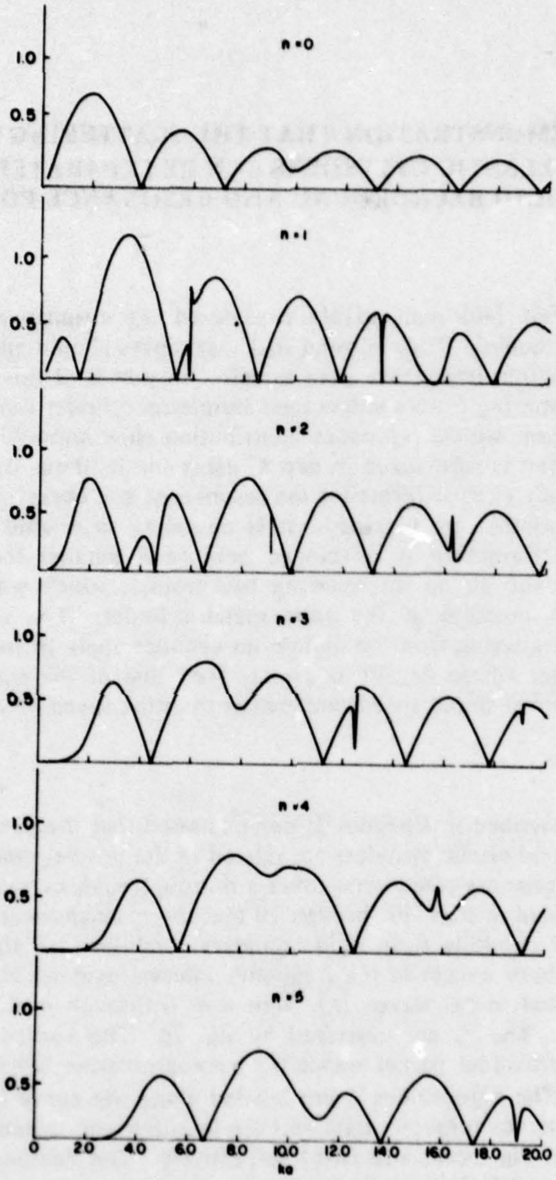

Fig. 17 – The individual partial wave amplitudes from n = 0 to n = 5 for the aluminum cylinder.

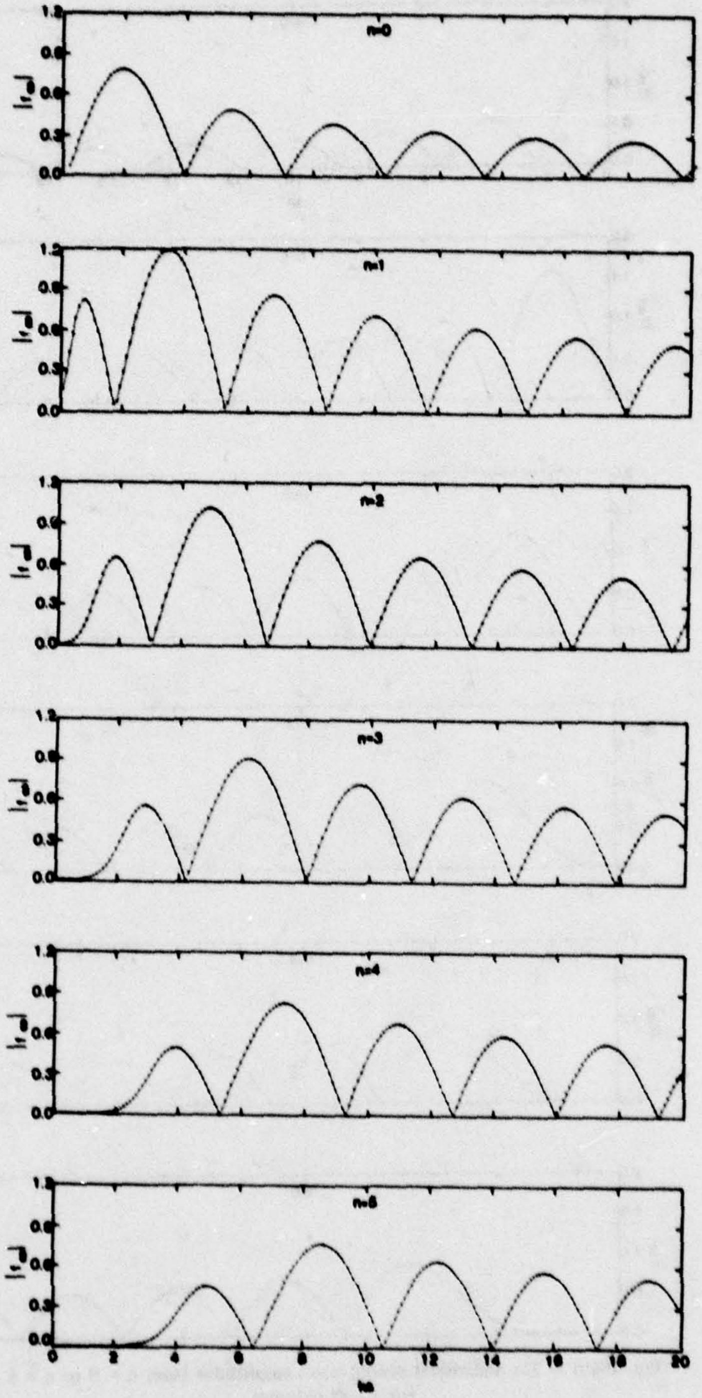

Fig. 18(a) – The individual parital wave amplitudes from n = 0 to n = 5 for a rigid cylinder.

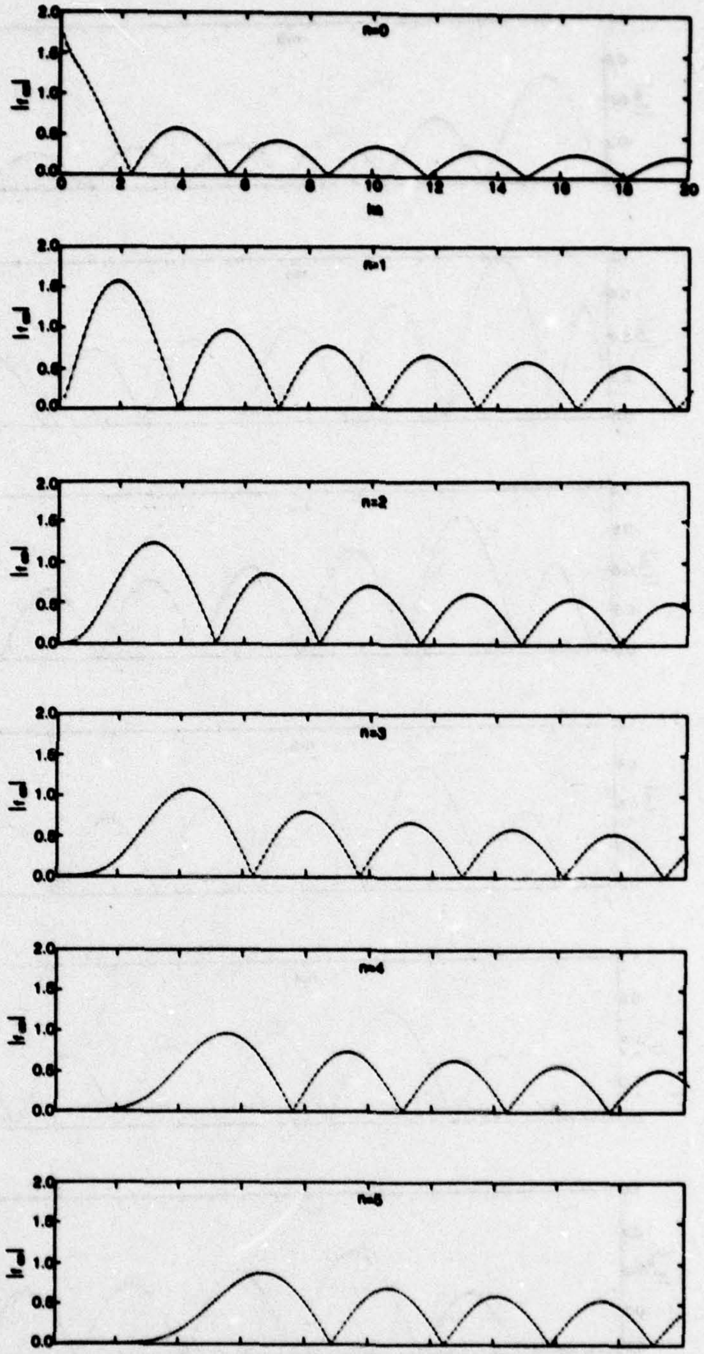

Fig. 18(b) – The individual partial wave amplitudes from n = 0 to n = 5 for a soft cylinder.

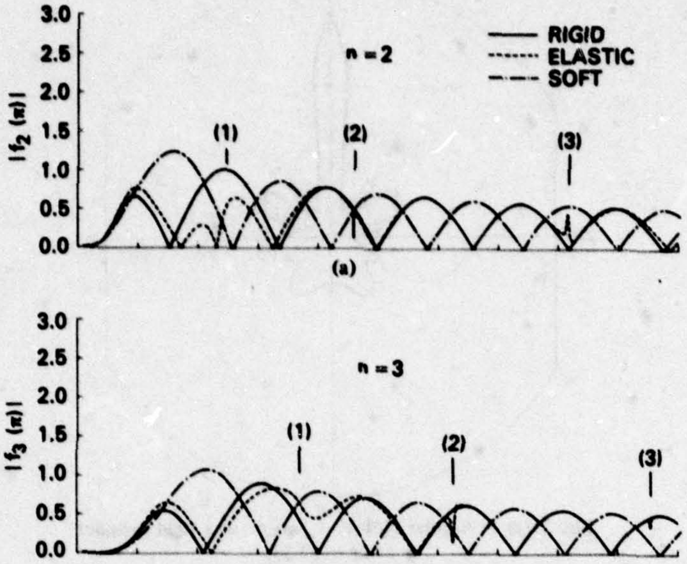

(a)

(b)

Fig. 19 – A comparison of the rigid (——), soft (– . –) and elastic (- - -) partial wave amplitudes for (a) n = 2 and (b) n = 3.

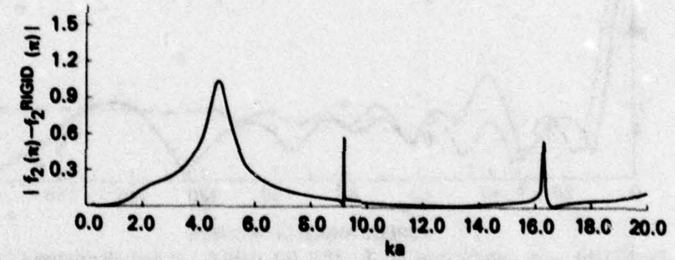

Fig. 20 – A plot of the difference between the elastic and rigid partial wave amplitudes for n = 2, over the range 0.2 ≤ ka ≤ 20.

computing resonance widths will be described in part C. The results seen in Figs. 17 through 20 are, of course, not restricted to the backscattered direction.

Fig. 21a shows a bistatic form function $|f_\infty(\theta)|$ curve for a rigid cylinder at $ka = 12.53$, which is the ka value at which the (3,2) resonance occurs in the aluminum case. In Fig. 21b this bistatic rigid form function is compared to the bistatic form function for an aluminum cylinder. Here the results are plotted on a linear rather than polar plot, and due to the symmetry apparent in Fig. 21a only the range $0° \leqslant \theta \leqslant 180°$ is plotted. The rigid and elastic solutions plotted in Fig. 21b were obtained with 23 terms ($n = 0$ through 22 from Eq. 7a). If the single $n = 3$ term from the elastic solution is substituted for the $n = 3$ term in the rigid solution, the result seen in Fig. 21c is obtained. A similar procedure was carried out by Vogt and Neubauer [41] for a sphere in a monostatic geometry. In Fig. 21c the exact bistatic solution for the aluminum cylinder at $ka = 12.53$ is compared to the hybrid solution formed by taking

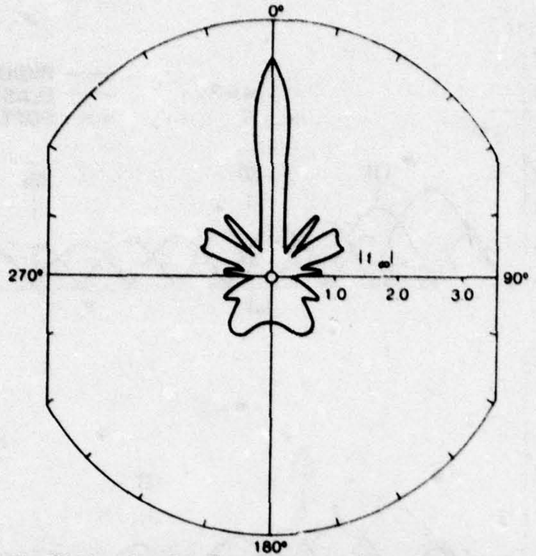

Fig. 21(a) – A polar plot of $|f_\infty|$ vs θ for a rigid cylinder at ka = 12.53.

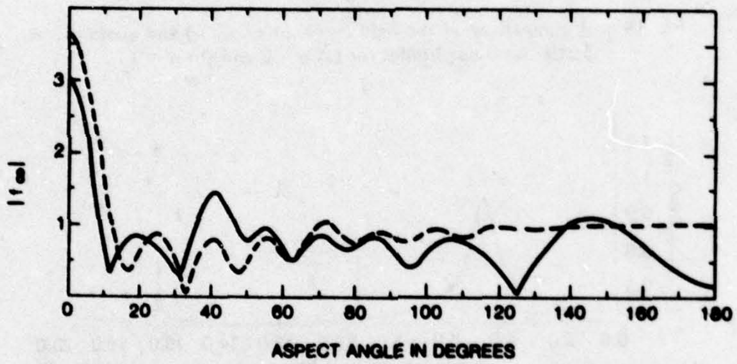

Fig. 21(b) – A comparison of $|f_\infty(\theta)|$ for rigid (- - -) and aluminum (–) cylinders at ka = 12.53.

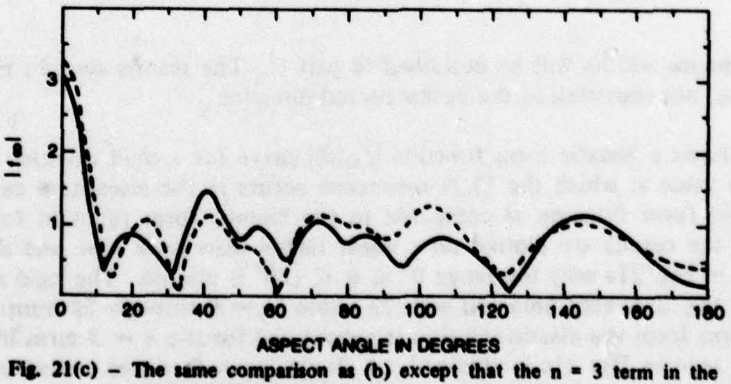

Fig. 21(c) – The same comparison as (b) except that the n = 3 term in the rigid series is replaced by the n = 3 elastic term.

22 terms from the rigid solution ($n = 0, 1, 2$, and $n = 4$ through 22) and adding the $n = 3$ term from the elastic solution. The modified-rigid form function vs aspect curve and the elastic form function curve seen in Fig. 21c have become similar. The differences between Figs. 21b and 21c are most noticeable in the backscattered half space, $90° < \theta < 270°$ (recall that by symmetry the results seen in Fig. 21c from $90° < \theta < 180°$ are exactly the same as the results between $180° < \theta < 270°$). Figure 21 again indicates the probability that the scattering from an aluminum cylinder can be treated as resulting from a rigid backgound term with resonances superimposed. It indicates further that this behavior is not limited to the single monostatic angle ($\theta = 180°$) but can be utilized at any bistatic aspect angle.

C. Mathematical formalism describing elastic resonance excitation

The results obtained in part B, indicate that the solution to the scattering from solid elastic bodies as expressed in Eqs. 4, 5, and 7 should be separable into two terms, the rigid backgound term and the resonance term. An analogy between the acoustic scattering problem and the existing resonance formalism of nuclear scattering theory was suggested by L. Flax and H. Überall, leading to the following.

If the scattering function

$$S_n \equiv \exp(2i\,\delta_n) \tag{32}$$

is introduced, the solution describing the scattering by an elastic cylinder may be written in the form familiar to nuclear reaction theory [42] as

$$p_s = 1/2 \sum_{n=0}^{\infty} \epsilon_n\, i^n (S_n - 1)\, H_n(kr) \cos n\theta. \tag{33}$$

The δ_n of Eq. (32) are called scattering phase shifts, and a comparison of Eqs. 1, 3, and 33 shows that

$$S_n - 1 = -2G_n(ka). \tag{34}$$

For the case of a rigid cylinder, defining ξ_n as the scattering phase shift for a rigid cylinder and defining

$$S_n^{(R)} \equiv \exp(2i\,\xi_n) \tag{35a}$$

as the scattering function for a rigid cylinder leads, using Eqs. 34 and 13, to

$$S_n^{(R)} - 1 = -2G_n^{(R)}(ka) \tag{35b}$$

and thus

$$S_n^{(R)} = \frac{H_n^{(2)\prime}(Z)}{H_n'(Z)}. \tag{35c}$$

If the rigid porition of the scattering function as given in Eq. 35c is factored out of the expression for the elastic scattering function Eq. (34), we have using Eqs. 3 and 35c

$$S_n = S_n^{(R)} \left\{ \frac{L_n^{-1} - z_2^{-1}}{L_n^{-1} - z_1^{-1}} \right\}. \tag{36}$$

The L_n's were previously defined in Eq. (1a), and the z's are defined by

$$z_1^{-1} = (Z)\,\frac{H_n(Z)}{H_n'(Z)} \tag{37a}$$

and

$$z_2^{-1} = (Z)\,\frac{H_n^{(2)}(Z)}{H_n^{(2)'}(Z)} \tag{37b}$$

the primes in Eqs. 37 and 35c represent derivatives with respect to the argument, and as defined previously H and $H^{(2)}$ are Hankel function of the first and second kind respectively. *The quantities z_i^{-1} of Eq. 37 can be separated into real and imaginary parts:*

$$z_{1,2}^{-1} = \Delta_n \pm i s_n \tag{38}$$

with

$$\Delta_n = 1/(Z)\,\frac{J_n(Z)\,J_n'(Z) + Y_n(Z)\,Y_n'(Z)}{[J_n'(Z)]^2 + [Y_n'(Z)]^2} \tag{39}$$

and

$$s_n = \frac{-2}{\pi Z^2}\left\{\frac{1}{[J_n'(Z)]^2 + [Y_n'(Z)]^2}\right\}. \tag{40}$$

Equation 36 may be rewritten using Eq. 38 as

$$S_n = S_n^{(R)}\left\{\frac{L_n^{-1} - \Delta_n + i s_n}{L_n^{-1} - \Delta_n - i s_n}\right\}. \tag{41}$$

The linear approximation method of nuclear resonance theory is used in which the resonance frequencies Z_n are defined by the condition

$$L_n^{-1}(Z_n) = \Delta_n. \tag{42a}$$

The quantity $(L_n^{-1} - \Delta_n)$ is assumed to be linearly varying with frequency so that it can be expanded in a Taylor series in Z in the vicinity of any one of the resonance frequencies:

$$L_n^{-1} \simeq \Delta_n + \beta_n (Z - Z_n). \tag{42b}$$

A resonance width is defined by

$$\Gamma_n = \frac{-2 s_n}{\beta_n} \tag{43}$$

and the scattering-function S_n, may be rewritten in resonance form as

$$S_n \equiv e^{2i\delta_n} = S_n^{(R)}\left\{\frac{Z - Z_n - i\Gamma_n/2}{Z - Z_n + i\Gamma_n/2}\right\}. \tag{44}$$

From Eq. 44 the S_n are seen to have resonance poles at the complex frequencies $Z = Z_{\text{pole}}$ given by

$$Z_{\text{pole}} = Z_n - \frac{1}{2}\, i\Gamma_n \tag{45}$$

and a resonance zero, $Z = Z_{zero}$, at

$$Z_{zero} = Z_n + \frac{1}{2}\, i\Gamma_n. \tag{46}$$

The resonance width Γ_n defined in Eq. 43 is a positive quantity. Thus Z_{pole} is located in the lower half of the complex Z-plane a distance $(1/2)\Gamma_n$ from the real axis, and Z_{zero} is located in the upper half plane at the same distance above the axis.

The quantity $S_n - 1$ which appears in Eq. 33 can be written, recalling the definition in Eq. 32, as

$$S_n - 1 \equiv 2i\, e^{i\delta_n} \sin \delta_n. \tag{46a}$$

Using Eq. 36 and the expressions for $z_{1,2}^{-1}$ given in Eq. 38 $(S_n - 1)$ can be rewritten in the form

$$S_n - 1 = 2i\, e^{i\xi_n} \left\{ \frac{s_n}{L_n^{-1} - \Delta_n - is_n} + e^{i\xi_n} \sin \xi_n \right\} \tag{46b}$$

or, using Eqs. 44 and 46a, $S_n - 1$ may be written in the resonance form

$$\frac{S_n - 1}{2i} = e^{2i\xi_n} \left\{ \frac{1/2\, \Gamma_n}{Z_n - Z - 1/2\, \Gamma_n} + e^{-i\xi_n} \sin \xi_n \right\}. \tag{47}$$

The individual partial waves, $f_n(\theta)$, of Eq. 7c can thus be written, using Eq. 47, as

$$f_n(\theta) = \frac{2i\, \xi_n}{(i\pi\, ka)^{1/2}}\, e^{2i\xi_n} \left[\frac{1/2\, \Gamma_n}{Z_n - Z - 1/2\, i\Gamma_n} + e^{-i\xi_n} \sin \xi_n \right] \cos (n\theta). \tag{48}$$

The first term of Eq. 48 represents the resonance contribution, and the second term represents the rigid boundary contributions; thus the results established in part B are expressed in a meaningful formalistic way. The representation of $f_n(\theta)$ given in Eq. 48 shows that the complex eigenfrequencies of the scatterers are the locations of the resonance poles in the complex frequency plane, whose real parts determine the resonance frequencies in the scattering amplitudes.

A consideration of the field within the elastic cylinder can also be made in light of the above results. The displacement **u** within the cylinder is represented by a scalar potential Ψ and a vector potential **A**, and is written

$$\mathbf{u} = -\Delta \Psi + \Delta \times \mathbf{A} \tag{49}$$

with solutions [20]

$$\Psi = \sum_{n=0}^{\infty} \epsilon_n\, i^n\, C_n\, J_n(k_L\, r) \cos n\theta \tag{50a}$$

and

$$A_Z = \sum_{n=0}^{\infty} \epsilon_n\, i^n\, B_n\, J_n(k_T\, r) \sin n\theta. \tag{50b}$$

The subscripts L and T are longitudinal and shear respectively. The coefficients C_n and B_n are given by

$$C_n = \frac{2i}{\pi\rho\, \omega^2}\, \frac{1}{Z H_n'(Z)\, D_n^{(1)}}\, \frac{a_{33}}{z^{-1} - L_n^{-1}} \tag{51a}$$

and

$$B_n = \frac{2i}{\pi \rho\, \omega^2} \, \frac{1}{Z H_n'(Z)\, D_n^{(1)}} \, \frac{a_{32}}{z^{-1} - L_n^{-1}}. \tag{51b}$$

The expansion of L_n^{-1} in Eq. 42 leads in to the resonance expressions for Ψ and A_z, which are

$$\Psi = \frac{2}{i\pi\, \rho\, \omega^2} \sum \frac{\epsilon_n\, i^n}{\beta_n} \, \frac{a_{33}}{Z H_n'(Z)\, D_n^{(1)}} \, \frac{J_n(k_L r) \cos n\phi}{Z - Z_n + 1/2\, i\Gamma_n} \tag{52a}$$

and

$$A_Z = \frac{2}{i\pi\, \rho\omega^2} \sum_{n=0}^{\infty} \frac{\epsilon_n\, i^n}{\beta_n} \, \frac{a_{32}}{Z H_n'(Z)\, D_n^{(1)}} \, \frac{J_n(k_T r) \sin n\phi}{Z - Z_n + 1/2\, i\Gamma_n}. \tag{52b}$$

Equations 52a and 52b show that the internal solutions are of a pure resonance form only. This is as expected, since by definition a rigid body is impenetrable; thus no rigid background term is expected for the internal solution.

V. CIRCUMFERENTIAL WAVES ON CYLINDRICAL SHELLS

A. Preface

Numerous [11-15,25-27] empirical observations of circumferential radiation from cylindrical shells exist in the literature, but these have left many serious voids in the understanding of circumferential waves as well as erroneous information concerning the properties of the waves. This chapter will establish the connection between circumferential waves and the exact Rayleigh series solution. It will demonstrate that the Lamb wave dispersion curves on plates predict the range of possible excitation of circumferential waves and that the velocity of circumferential waves may be obtained directly from the form function vs *ka* curves. It is shown that these Lamb curves also give immediate knowledge of the *ka* region over which a particular circumferential mode is significant. Calculations of the backscattered echoes from shells will be used to obtain curves relating the amplitude of the specular and circumferential contributions as a function of *ka*, and, contrary to the prevalent belief expressed in the literature, the circumferential waves will be shown to be of most importance in the low *ka* region generally avoided in past work. A target classification scheme was proposed in the literature which relied on the assumption that a hollow shell acts as a soft body, in that its specular reflection is 180° out of phase with an incident wave [43]. By consideration of the interference between specular and circumferential radiation, the actual *ka* range over which such a hypothesis is valid is determined.

Most of the pertinent references on the subject of circumferential waves on cylindrical shells have been mentioned in Chapter I. They and others are discussed in more detail below, where they are considered, generally, in chronological order. Barnard and McKinney [11] were the first to observe backscattered acoustic echoes with circumferential properties. This observation was a significant contribution. They attempted to link the observed acoustic phenomenon to the geometric diffraction phenomenon observed by Franz [18] in the electromagnetic domain; however, the analogy broke down, since the acoustic phenomenon was a predominately elastic effect, the geometry serving in the capacity of a waveguide. Horton, King, and Diercks [13] made the initial attempt to relate circumferential waves on cylindrical shells to the elastic properties of flat plates. They compared their observation of a circumferential wave on an aluminum shell to a theoretically computed flexural plate mode and found a 10% difference between measured and predicted velocities. A similar comparison was attempted with a brass shell [13], but the circumferential wave could not be excited. The *ka* range considered was $21 < ka < 38$, with $b/a = 0.96$, where b and a are the inner and outer shell radius respectively. The circumferential wave observed by Horton et al. will be related in this work to the first antisymmetric Lamb mode, whose properties and *ka* region of possible excitation are discussed later. Diercks, Goldsberry, and Horton [12] made empirical observations of circumferential waves on both brass and aluminum shells near $ka \simeq 50$, with $b/a = 0.96$. They established the existence of circumferential waves with two different group velocities. The faster velocity wave was called a longitudinal mode, and the lower velocity wave was called the flexural mode. This paper by Diercks et al. [12] was significant in that it was the first to clearly state that more than one circumferential mode existed. Their conclusions, concerning which mode is dominant and whether both modes can be simultaneously excited, were thought to be general but are limited strictly to the conditions of the observations. It will be demonstrated in part C of this chapter that the so-called longitudinal mode is actually many different modes, and herein lies much of the confusion about the frequency range of excitation and/or dominance of a particular mode. Goldsberry [14] demonstrated that the circumferential waves observed previously at DRL [11-13] would reflect from slits cut in the shell. He called the wave with lower group velocity a low frequency wave, and the faster wave a high frequency wave. Again these generalizations do not survive beyond the experimental conditions. The ranges he considered were $32 < ka < 38$ (flexural, slow, low frequency wave) and $70 < ka < 76$ (compressional, fast, high frequency wave). The b/a was 0.96. Uberall and collaborators at Catholic University predicted circumferential waves of different types on rigid [20] and elastic cylinders [21] and shells [44]. These predicted wave types were Franz-type waves [20] with properties similar to the electromagnetic case of Franz [16], and R-type or Rayleigh-type [21,44] waves, which depend on the elastic properties of the target. Neubauer [23] empirically isolated the Franz-type wave on a solid elastic cylinder in water, and Harbold and Steinberg [24] isolated the wave on a rigid cylinder in air.

Bunney, Goodman, and Marshall [25] used narrow beam sources to illuminate cylindrical shells over narrow ranges of incidence angles and directional receivers to observe circumferential-wave radiation. The ka range they considered was between $50 < ka < 320$ with $b/a = 0.95$. Many observations of a low velocity circumferential wave were compared to the antisymmetric Lamb mode, and the single observation of a higher velocity mode was related to the symmetric plate mode.

Neubauer and Dragonette [27] and Dragonette [45] empirically demonstrated that the velocity of the observed circumferential waves on cylindrical shells [27] and the velocity of Lamb waves on plates [45] could be predicted by considering guided wave propagation within cylindrical shells and plates. Dragonette [45] also established that Lamb modes were most easily excited in the frequency thickness regions where the phase velocity reached a constant plateau. This result is significant in a consideration of the so-called fast circumferential wave on cylindrical shells, as will be seen in part C, and is the basis for correcting some erroneous conclusions in the literature.

Shirley and Diercks [46] compared measured and predicted values of the steady state response of spherical shells over the range $25 < ka < 65$ with $b/a = .95$. Differences of the order of 10 dB, or a factor of 300% in pressure amplitude, were found between theory and prediction, but similarities in shape between the theoretical and empirical curves were observed.

Horton and Mechler [15] attempted to measure phase velocity of circumferential waves on aluminum cylindrical shells by setting up a long pulse or steady state interference pattern between the successive circumferential pulses. The significance of their paper was that it offered a possible approach to phase velocity determination which, as will be discussed later, is a difficult parameter to obtain when waves are excited on a curved surface.

B. Experimental observation and analysis of the properties of circumferential waves on shells

Figure 22 shows the geometry of the cylindrical shell problem. It is similar to Fig. 1 except that the target now has a finite thickness h given by $h = a - b$, where b is the inner radius and a is the outer radius. The shell is air filled. An experimental observation of circum-

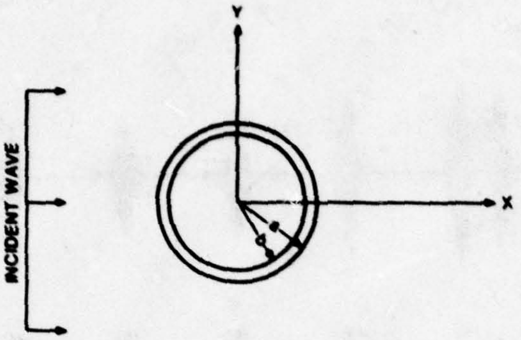

Fig. 22 – The geometry used in the solution to the reflection from a cylindrical shell.

ferential waves is seen in Fig. 23. Here the target is a stainless steel cylindrical shell with $b/a = 0.96$. The radius of the shell is 1.27 cm, and the center frequency of the pulses seen in Fig. 23 is 1.5 MHz, leading to $k_o\, a = 80$. The specular reflection is not shown, as it is 40 dB greater than the largest echo seen in Fig. 23, and was gated out of the return so that the echoes seen in the figure could be amplified to the maximum extent before display. The backscattered echo seen in Fig. 23 was obtained using the experimental system described in Appendix B. The source/receiver is located 15 diameters from the target. The backscattered echo seen in Fig. 23 was digitized at the rate of 13 points per cycle and stored on magnetic tape. The representation seen in Fig. 23 was obtained with a Versatec plotter. The first, third, and all successive echoes in Fig. 23 result from a circumferential wave which circumnavigates the cylinder, with little attenuation, continually radiating into the water as it travels. The second echo in Fig. 23 is the result of a second type of circumferential wave so highly attenuated at the ka and/or kh value of this experiment that only its first traversal around the cylinder is observed before it attenuates into the noise. (Observation of Fig. 23 alone would not allow identification of the second echo as a circumferential wave. This identification was based on many experimental measurements, some of which will be seen below.) Measurements of the circumferential velocity of the persistent series of equally spaced echoes (1-7) in Fig. 23 are straightforward. The circumferential group velocity c_g^* is obtained from Fig. 23 by

$$c_g^* = \frac{2\pi a}{\Delta t}$$

where Δt is the time between echoes and $2\pi a$ is the circumference of the shell. The measured value from Fig. 23 is $c_g^* = 5.48 \times 10^5$ cm/s or $c_g^*/c = 3.7$. This value for c_g^* identifies this wave as that previously called the "fast", "high frequency", or "compressional" wave by previous observers [13-15]. As will be discussed, these names can be misleading or in error. Attenuation measurements from Fig. 23 are also straightforward. The successive amplitudes from Fig. 23 are plotted on semilog paper in Fig. 24, yielding an attenuation of

$$\alpha_g^* = 0.14 \text{ Np/revolution.}$$

The use of the digitizing procedure and display makes possible observation of the individual cycles of the successive echoes in Fig. 23. The empirical observations which follow in Figs. 25 through 28 are simply photographs of scope traces, and the time scale needed to show many successive echoes does not allow observation of the individual cycles within the echo.

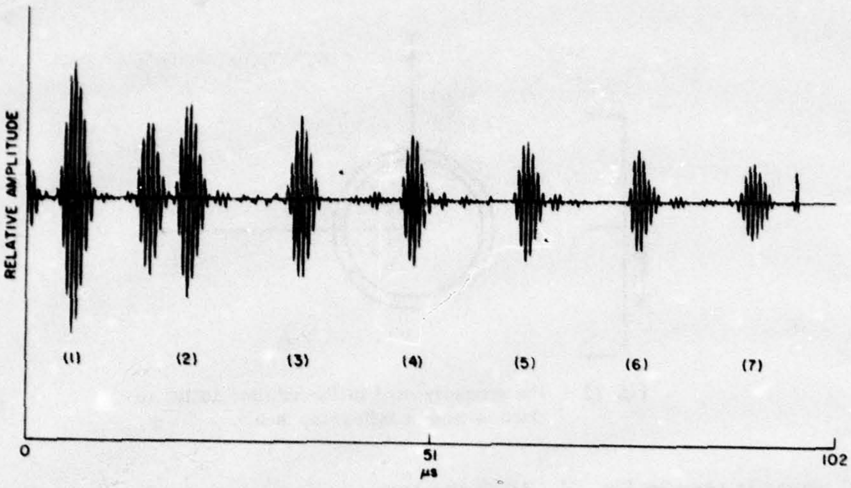

Fig. 23 – Experimental observation of circumferential waves on a stainless steel at $k_0a = 80$.

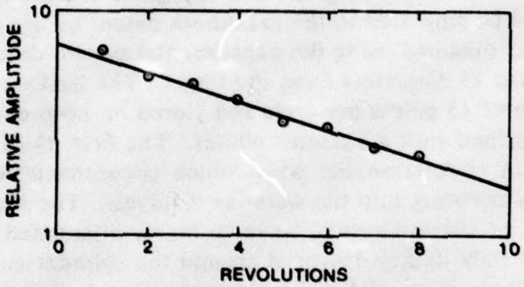

Fig. 24 – The amplitude of the circumferential waves seen in Fig. 23 plotted on semilog paper.

Fig. 25 – Experimental observation of a "fast" circumferential wave at $k_0a = 11$, on a stainless steel shell. The time scale is 20μs/division; the amplitude scale is 5 mv/division.

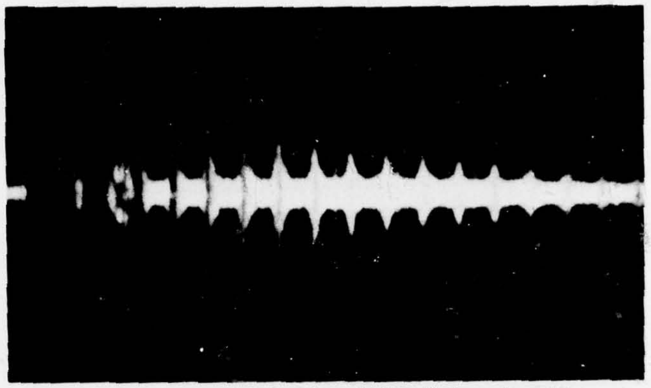

Fig. 26 – Experimental observation of a "fast" circumferential wave at $k_0a = 69$, on a stainless steel shell. The time scale is 20μs/division; the amplitude scale is 2 mv/division.

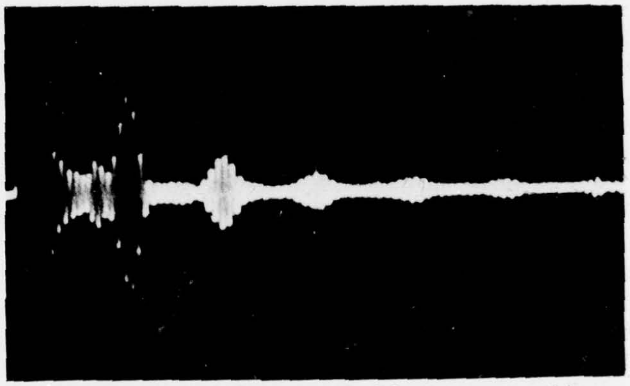

Fig. 27 – Experimental observation of a "slow" circumferential wave at $k_0a = 17$, on a stainless stell shell. The time scale is 20μs/division; the amplitude scale is 200 mv/division.

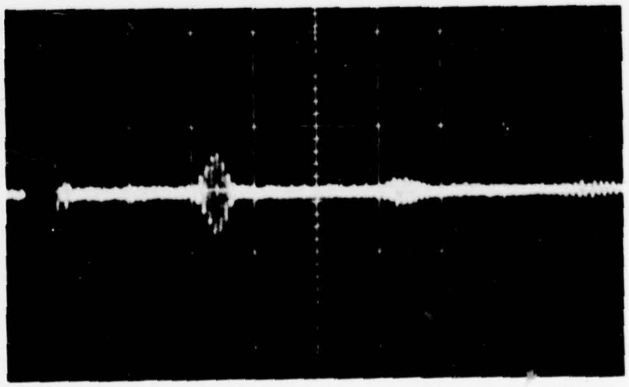

Fig. 28 – Experimental observation of a "slow" circumferential wave at $k_0a = 43$, on a stainless steel shell. The time scale is 20μs/division; the amplitude scale is 2 mv/division.

Figures 25, 26, 27, and 28 show further results of reflection measurements on steel shells, and the experimental conditions and results are summarized in Table III, which also includes the results described for Fig. 23.

Table III
Summary of cylindrical shell observations

Figure	Radius (cm)	$k_0 a$	b/a	c_g/c	α^* Np/revolution
23	1.27	80.8	.96	3.7	0.142
25	1.59	113.0	.97	3.5	0.209
26	0.9525	69.0	.95	3.6	0.126
27	0.9525	17.0	.95	1.35	1.000
28	1.905	43.0	.97	1.35	0.600

The hydrophone measurements seen in Figs. 23 and 25 through 28 show the acoustic reflection in the backscattered direction, $\theta = 180°$. Observation of the entire scattered field, $0 \leqslant \theta \leqslant 2\pi$ can be obtined simultaneously by schlieren visualization. Figure 29 shows a schlieren visualization of the scattered field of a stainless steel cylindrical shell of radius 0.9525 cm with $b/a = 0.95$. The $k_0 a$ of the experiment is 202. The incident pulse is seen in Fig. 29a, and the time sequence of photographs shows the scattered field at later times. The specular reflection and the beginning of the radiation from a circumferential wave are seen in Fig. 29b, and Fig. 29c shows the reradiation from the first complete traversal of the circumferential wave into the backscattered direction. At the bottom of Fig. 29c the diffraction around the shell can also be observed. The group velocity of the wave seen in Fig. 29 is $c_g'/c = 3.6$. In Fig. 29 the incident pulse insonified the entire cylinder, so that the same effect was generated on both the upper left and upper right quadrants of the cylinder.

The properties of the circumferential waves seen in Figs. 23 and 25 through 29 are similar to circumferential wave properties previously reported in the literature [11-15,25-27]. Specifically, circumferential waves with group velocities $c_g'/c \simeq 3.6$ (Figs. 23, 25, and 26) and $c_g'/c \simeq 1.3$ (Figs. 27 and 28) are observed, with the faster group velocity observed at the higher frequency (or higher ka) and the slower group velocity wave at the lower frequency. This simple interpretation of the results is, however, misleading and demonstrates some of the practical difficulties in a predominantly empirical approach to this problem, where broad generalizations are made, based on limited measurements. The experimental measurements here, and reported previously, are generally made at high ka values. At very low frequencies, or ka values below $ka = 20$, it is a practical impossibility to achieve short enough pulse lengths to separate circumferential waves with transducers generally available; hence, high ka measurements are made as a matter of necessity. This low-ka limitation on the isolation of separate echoes is especially true of high speed circumferential waves. In addition, most empirical measurements are made on shells with $b/a \leqslant 0.96$, since thinner shells are more difficult to fabricate and maintain. Finally, as a practical matter it is not possible to measure enough combinations of shells and freqencies to do a complete empirical study. This latter statement is true not only because of the low ka separation difficulty mentioned above but also because in the case of a curved shell there are two frequency variables. For a flat plate, frequency times thickness, fh may be considered a single variable. The radiation from a given plate may be examined as a function of

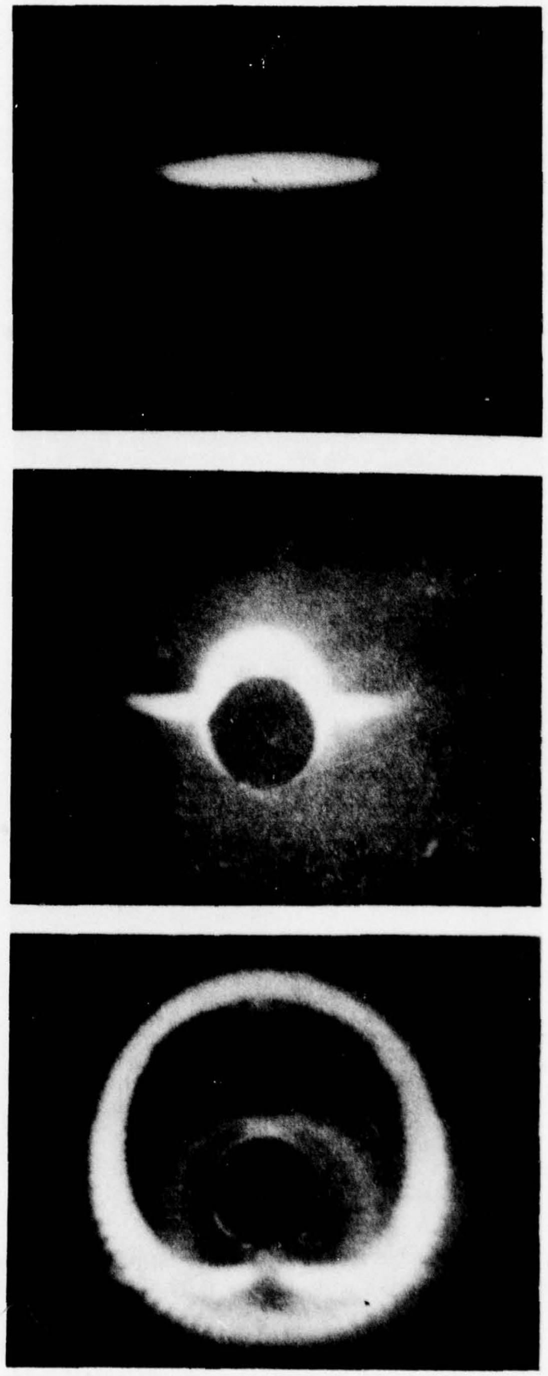

Fig. 29 – Schlieren visulization of a "fast" circumferential wave at $k_0a = 202$ on a stainless steel shell.

fh simply by varying the frequency of the incident pulse or continuous wave. A similar experiment on a curved shell is not as unambiguous. As the frequency of the incoming wave is varied, the *fh* or *kh* of the shell changes accordingly, but in addition the *ka* value changes. As will be seen, there are certain effects which are strong functions of *ka*, and others which depend almost entirely on *kh*. These had not previously been differentiated successfully in the literature, and this could not have been reasonably accomplished empirically. Because previous work has been limited to the high *ka* region, where the flat surface limit is approached, the *kh* variable has generally been considered most significant in all empirical observations of isolated circumferential waves. In fact the low *ka* region which has been avoided is the only *ka* region where a high velocity circumferential wave plays a significant role in the acoustic scattering by a cylindrical shell, as will be demonstrated.

C. Theoretical normal mode formulation of the shell problem

Analysis of circumferential waves on cylindrical shells can best be accomplished by determining the relationship between the circumferential waves and exact steady state theory. In addition, as will be seen in part D, Lamb theory for plates can be used to predict the possible ranges of excitation of circumferential waves on shells.

The geometry of the cylindrical shell problem was given in Fig. 22. The formulation of the exact normal mode solution to the scattering of sound by an elastic cylindrical shell exists in the literature and can be presented in a form similar to that of Eq. 1, which described the scattering from solid elastic cylinders [32]:

$$p_s(\theta) = -p_0 \sum \epsilon_n (i)^n \left\{ \frac{J_n(Z)\, Q_n - Z\, J_n'(Z)}{H_n(Z)\, Q_n - Z\, H_n'(Z)} \right\} H_n(kr) \cos n\theta. \tag{53}$$

This expression differs from Eq. (1) only in the replacement of L_n, which involved the division of two 2-by-2 matrices, by Q_n, which involves the division of two 4-by-4 matrices. The larger matrix results from the extra boundary condition on the surface $r = b$, and the expression for Q_n is

$$Q_n = \frac{\rho}{\rho_s} \; \frac{\begin{vmatrix} a_{21} & a_{22} & a_{23} & a_{24} \\ a_{31} & a_{32} & a_{33} & a_{34} \\ a_{41} & a_{42} & a_{43} & a_{44} \\ a_{61} & a_{62} & a_{63} & a_{64} \end{vmatrix}}{\begin{vmatrix} a_{11} & a_{12} & a_{13} & a_{14} \\ a_{31} & a_{32} & a_{33} & a_{34} \\ a_{41} & a_{42} & a_{43} & a_{44} \\ a_{61} & a_{62} & a_{63} & a_{64} \end{vmatrix}} \tag{54}$$

with the matrix elements a_{ij} given in Ref. 32. Computations are given in Fig. 30 of the form function vs *ka* for stainless steel shells with $b/a = 0.99$ (Fig. 30a) and $b/a = 0.98$ (Fig. 30b). The curves cover the *ka* range $0.2 \leqslant ka \leqslant 50$. A similar set of curves for aluminum are given in Fig. 31, and the two figures demonstrate the similarity of results obtained on metals quite different in density, but with shear and longitudinal speeds approximately twice and four times the water speed, respectively. The elastic constants used in obtaining the curves seen in Figs. 30 and 31 are given in Appendix C.

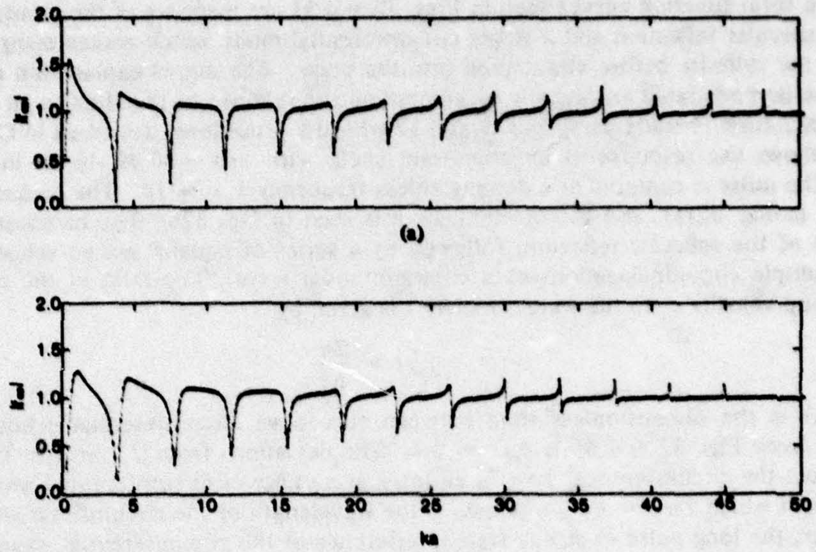

(a)

(b)

Fig. 30 – The form function for stainless steel shells over the range 0.2 ≤ ka ≤ 50 for shell thickness of (a) 0.99 and (b) 0.98.

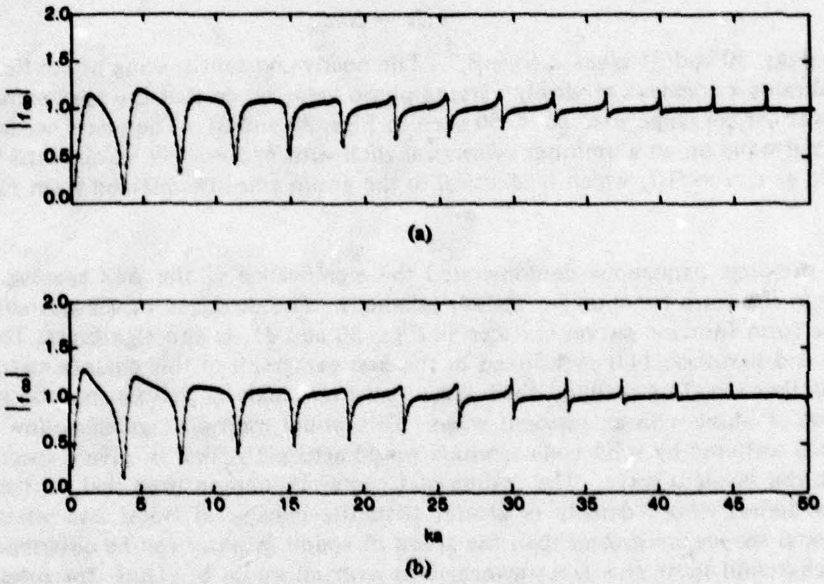

(a)

(b)

Fig. 31 – The form function for aluminum shells over the range 0.2 ≤ ka ≤ 50 for shell thicknesses of (a) 0.99 and (b) 0.98.

The form function curves seen in Figs. 30 and 31 are made up of the steady state interference of specular reflection and a single circumferential mode which makes many circumnavigations of the cylinder before attenuating into the noise. The above explanation of Figs. 30 and 31 can be demonstrated analytically by computing the reponse of the shell to an incident pulse. The computation is made using Eqs. 9 and 12 with the procedures described in Chapter II. Figure 32 shows the response of an aluminum shell, with $b/a = 0.99$, to an incident acoustic pulse. The pulse is centered at a dimensionless frequency $k_0 a = 10$. The backscattered echoes are seen in Fig. 32(a), and the incident wave is seen in Fig. 32b. The backscattered return is made up of the specular reflection followed by a series of equally spaced echoes which result from multiple circumnavigations of a circumferential wave. The ratio of the circumferential-wave group velocity c_g^* to the water velocity c is given by

$$c_g^*/c = \frac{2\pi}{\Delta\tau} \tag{55}$$

where $\Delta\tau$ is the dimensionless time between successive circumferential echoes. The result obtained from Eqs. 32 and 55 is $c_g^*/c = 3.7$. The deviations from $|f_\infty| = 1$ in Figs. 30 and 31 occur when the circumference, $2\pi a$, is an integral number of circumferential wavelengths. For ka values at which $2\pi a = n\lambda^*$, where λ^* is the wavelength of the circumferential wave and n is an integer, the long pulse or steady state interference of the circumferential waves gives a maximum contribution, since all add in phase with one another. At these ka values peaks will occur in the form function if the specular reflection and circumferential waves are in phase and nulls will occur if they are out of phase. The ka difference, Δka, between the successive fluctuations in the $|f_\infty|$ vs ka function are directly related to the circumferential wave phase velocity c_p^* by

$$c_p^*/c = \Delta ka \tag{56}$$

which for Figs. 30 and 31 gives $c_p/c = 3.7$. The nearly constant spacing of the fluctuations $\Delta ka \simeq 3.7$ indicates a constant or slowly varying phase velocity, so that the approximation $c_g^* \simeq c_p^*$ is valid over the ka range $0 < ka < 50$ seen in Figs. 30 and 31. The phase velocity of the circumferential wave on an aluminum cylindrical shell with $b/a = 0.99$, is obtained from Fig. 31a and Eq. 56 as $c_p/c = 3.7$, which is identical to the group velocity obtained from Fig. 32 and Eq. 55.

The previous paragraphs demonstrated the significance of the Δka spacing between the deviations in the form function for cylindrical shells. The direction of the deviations from $|f_\infty| = 1$ in the form function curves, as seen in Figs. 30 and 31, is also significant. The hypothesis of Tucker and Barnickle [43] mentioned in the first paragraph of this chapter was based on the assumption that a hollow air-filled shell will act as a soft body in that its specular reflection will be 180° out of phase with an incident wave. This would then distinguish hollow body echoes from echoes scattered by solid bodies, which would act rigidly, that is, give a specular return in phase with the incident wave. The results of Chapter IV demonstrate that, in fact, the return from solid bodies whose density is greater than the density of water and whose shear and compressional speeds are greater than the speed of sound in water can be described in terms of a rigid background term plus a resonance term over all $ka > 0$. Thus, for solid bodies with these elastic properties, the rigid background portion of the hypothesis of Tucker and Barnickle would be correct. With regard to the "soft" scattering by a hollow shell, however, the hypothesis breaks down, as can be determined form the work described in the previous paragraph. Figures 30 and 31 demonstrate that the ka range over which cylindrical shells will act as a soft body is a function of frequency. As frequency is increased, the thickness h of a given

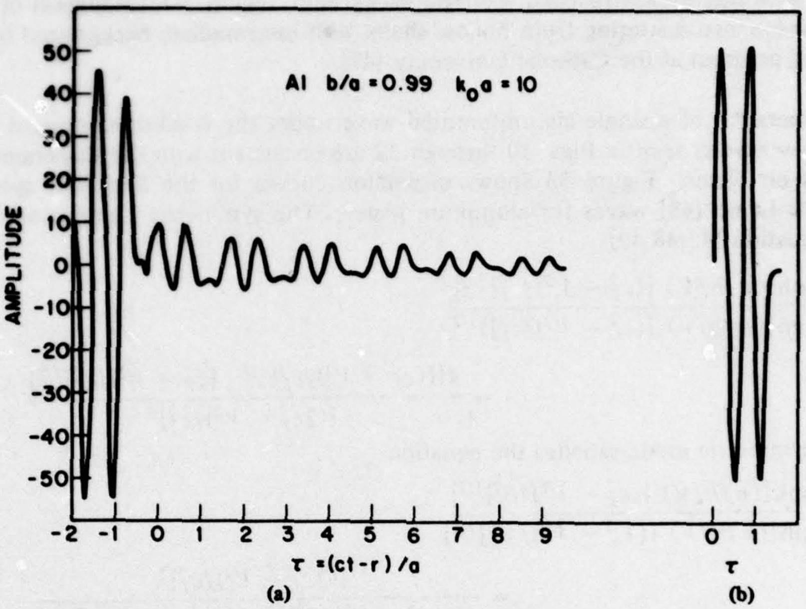

Fig. 32 – Computations of the echoes (seen in (a)) scattered when a short incident pulse (seen in (b)) impinges on aluminum shell with b/a = 0.99. The pulse is centered at $k_0a = 10$.

shell becomes greater with respect to a wavelength, and whether a shell acts as a "soft" body (specular reflection 180° out of phase with the incident wave) or a "rigid" body (specular reflection in phase with the incident wave) depends both on the frequency and shell thickness. For example, as was discussed, the fluctuations in $|f_\infty|$ for the shell described in Fig. 31b occur at intervals $\Delta ka \simeq 3.7$. The deviations from $|f_\infty| = 1$ are, however, not uniform in direction either in Fig. 31b or in any of the other form function curves shown in Figs. 30 and 31. Three separate background regions exist.

The shell acts as a soft body over the ka range where the fluctuations in $|f_\infty|$, at $\Delta ka =$ 3.7, are in the negative direction. Here the specular and incident wave are 180° out of phase. Recall that the incident wave and the circumferential wave are in phase (as seen in Fig. 32), and further pulse calculations such as that in Fig. 32 show that they remain in phase over the ka range from $0.2 \leqslant ka \leqslant 50$. For an aluminum shell with $b/a = 0.98$ the ka region over which the shell acts as a "soft" body (specular reflection and the incident wave 180° out of phase) is seen from Fig. 31b to be $0 \leqslant ka \leqslant 23$.

As ka increases, the shell passes through a transition region during which a single fluctuation has both positive and negative aspects. This occurs over the range $23 \leqslant ka \leqslant 37$ for the 0.98 aluminum shell. Finally for $ka > 40$ the deviations from $|f_\infty| = 1$ are positive and the shell is a rigid reflector with respect to its specular reflection. The extent in ka of the three background regions will vary with thickness and with material. Later in this section the advent of higher order modes will be discussed, but it can generally be said that if the product of frequency and thickness is large enough to allow more than one circumferential mode to be excited, the shell has already reached the rigid background region. Development of the formalism for the resonance scattering from hollow shells with intermediate background is the subject of an ongoing program at the Catholic University [47].

The generation of a single circumferential wave under the conditions present in the computation of the results seen in Figs. 30 through 32 are consistent with the dispersion curves for Lamb waves on plates. Figure 33 shows dispersion curves for the first four symmetric and antisymmetric Lamb [48] waves for aluminum plates. The symmetric Lamb modes satisfy the frequency equation [45,48,49]

$$\frac{\tanh\{(\pi fh/V)\,[(c_T^2 - V^2)/c_T^2]^{1/2}\}}{\tanh\{(\pi fh/V)\,[(c_L^2 - V^2)/c_L^2]\}^{1/2}} = \frac{4\{[(c_L^2 - V^2)/c_L^2]^{1/2}\cdot[c_T^2 - V^2)/c_T^2]^{1/2}\}}{[(2c_T^2 - V^2)/c_T^2]^2} \tag{57}$$

and the antisymmetric mode satisfies the equation

$$\frac{\tanh\{(\pi fh/V)\,[(c_T^2 - V^2)/c_T^2]^{1/2}\}}{\tanh\{(\pi fh/V)\,[(V_p^2 - V^2)/V_p^2]^{1/2}\}} = \frac{[(2c_T^2 - V^2)/c_T^2]^2}{4\{[(c_L^2 - V^2)/c_L^2]^{1/2}\cdot[(c_T^2 - V^2)/c_T^2]^{1/2}\}}. \tag{58}$$

In Eqs. 57 and 58, V is the Lamb phase velocity. The group velocity of the Lamb wave, V_g, is related to the phase velocity by

$$V_g = V\left[1 - \frac{1}{1 - (fh)\,dV/d(fh)}\right]. \tag{59}$$

It has been demonstrated that Eqs. 57 through 59 describing Lamb waves on plates in vacuo are not strongly modified when the plate is immersed in water [45,49,50] and that Lamb waves can be generated by illuminating a plate in water by an incident pulse [45,49]. Radiation of the Lamb wave into the water can be observed either with a hydrophone [49] or by schlieren visualization [45].

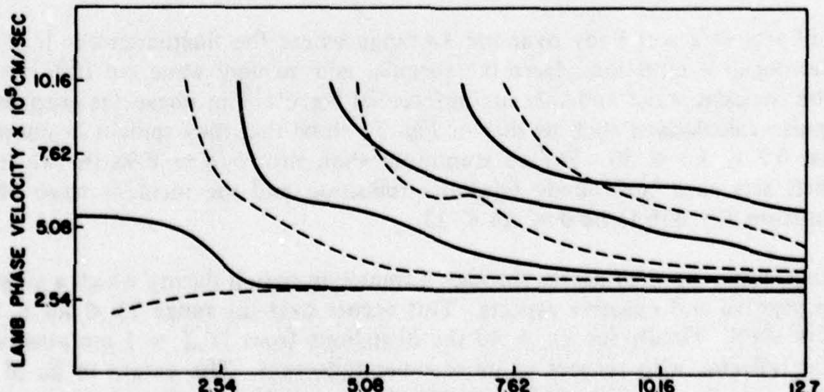

Fig. 33 – The Lamb dispersion curves for the first four symmetric (——) and antisymmetric (- - -) Lamb waves on aluminum plates.

Grigsby and Tajchman [51] gave dimensionless curves for the phase and group velocities of Lamb waves on a plate whose ratio of longitudinal to shear speeds is 1.8. Their curves are seen in Fig. 34. Special attention is directed to the group velocity curves in Fig. 34b, where all the modes show a flat peak in the group velocity at $V_{gn} \simeq 1.8$. In Fig. 34 the ordinate V_n is Lamb phase velocity divided by shear velocity i.e. $V_n = V/c_T$, and the abscissa $(fh)_n$ is fh/c_T. In Fig. 34b the ordinate $V_{gn} = V_g/c_T$.

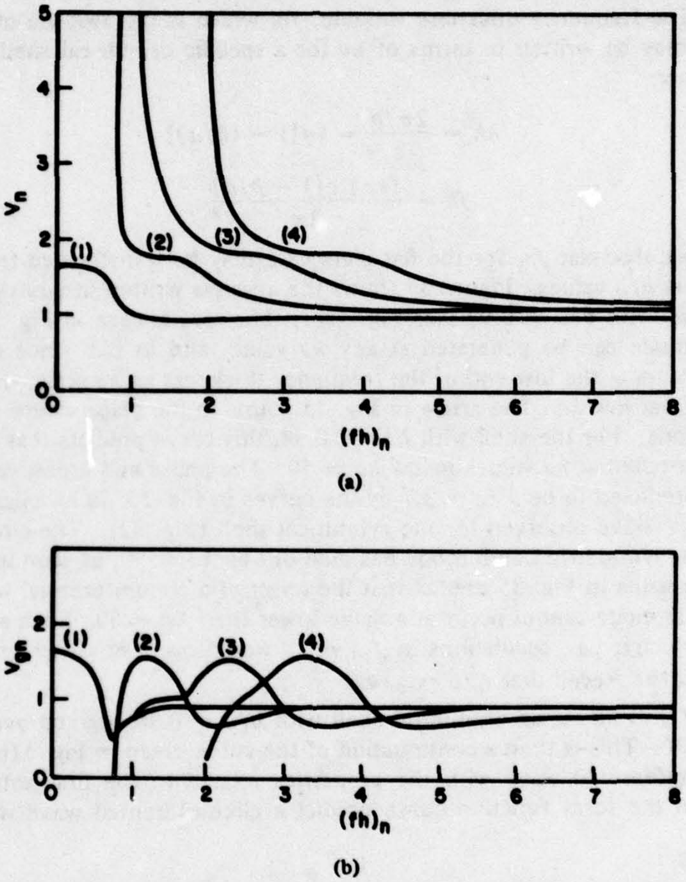

Fig. 34 – Dimensionless curves of (a) Lamb phase velocity and (b) Lamb velocity curves for materials with $c_L/c_T = 1.8$.

Dragonette [45] demonstrated that strong generation of a Lamb mode takes place in the region where the phase velocity curves reach a flat plateau (at approximately $V_n = 1.8$ in Fig. 34a). This plateau region corresponds to the frequency thickness region where the group velocity curve for a particular mode reaches a flat maximum (at approximately $V_{gn} = 1.8$ in Fig. 34b). Dragonette [45] demonstrated further that this stong generation of a Lamb mode, in the *fh* region where phase velocity is approximately equal to the group velocity, persisted as the plate was curved.

In Fig. 35 the Lamb phase velocity curves describing the first symmetric and first antisymmetric curves for an aluminum plate are isolated. The ordinate is given in terms of the Lamb phase velocity V, and also in terms of the angle of incidence θ_i at which a Lamb wave, with that phase velocity, can be generated by a plane wave incident from water on to the plate surface. This angle θ_i satisfies the equation

$$\sin \theta_i = c/V, \tag{60}$$

and a Lamb mode cannot be generated by an acoustic wave incident from water to the plate unless $V > c$. The frequency thickness variable, fh, which is the abscissa of the Lamb curves seen in Fig. 35 may be written in terms of ka for a specific cylindrical shell by a simple algebraic manipulation:

$$kh = \frac{2\pi fh}{c} = ka[1 - (b/a)] \tag{61a}$$

$$fh = \frac{(ka)\, c(1 - b/a)}{2\pi}. \tag{61b}$$

Using Eq. 61b the abscissa, fh, for the flat plate case may be transformed from fh into ka for shells with various b/a values. Figure 35 shows the abscissa written in equivalent ka values for an aluminum shell with $b/a = 0.98$ (see Fig. 31b). The results seen in Fig. 35 predict that the first symmetric mode can be generated at any ka value, and in fact since the flat plateau in group velocity occurs at the low end of the frequency thickness or ka scale, this wave should be strongly generated at low ka. The arrow in Fig. 35 points to the place where $V = c$ for the first antisymmetric mode. For the shell with $b/a = 0.98$, this curve predicts that the antisymmetric mode cannot be excited at ka values below $ka \simeq 50$. The phase and group velocity of the symmetric mode is predicted to be $V/c = 3.7$ by the curves in Fig. 35, in excellent agreement with the circumferential wave observed for the cylindrical shell (Fig. 32). The circumferential wave related to the first symmetric Lamb mode has died out by $ka \simeq 50$, as seen in Fig. 31b, and, as seen above, the results in Fig. 35 predict that the onset of a circumferential wave related to the first antisymmetric mode cannot occur at a value lower than $ka = 50$. Such a wave would have a lower group velocity; i.e., oscillations in $|f_\infty|$ vs ka would occur at closer intervals than those observed in Fig. 31b. Recall that $c_p^*/c = \Delta ka$.

A plot of $|f_\infty|$ vs ka for an aluminum shell with $b/a = 0.98$ is given over the range $50 \leq ka \leq 90$ in Fig. 36. This is then a continuation of the curve given in Fig. 31b, and it shows the onset of a circumferential wave with the properties related to the first antisymmetric mode. The oscillation in the form function curve predict a circumferential wave with $c_p^*/c = \Delta ka = 1.3$.

In general, then, a circumferential wave related to the first symmetric mode should always be generated for a shell of any thickness. Its influence is restricted to the low ka region over which the phase velocity has a flat plateau. This region is a function of thickness, as will be described below. A circumferential wave related to the first antisymmetric mode can only be generated at ka values higher than the coincidence frequency $ka = (ka)_c$, where $V = c$. Thus the thicker the shell, the lower the ka value at which this mode can be generated.

These conclusions should be reflected in the form function curves for aluminum cylindrical shells of various thicknesses. Differences from $|f_\infty| = 1$ should occur at intervals $\Delta ka \simeq 3.7$ for all thin shells, and these differences should die out more quickly with ka as thickness increases, since the plateau region in Fig. 35 corresponds to a smaller ka range for thicker

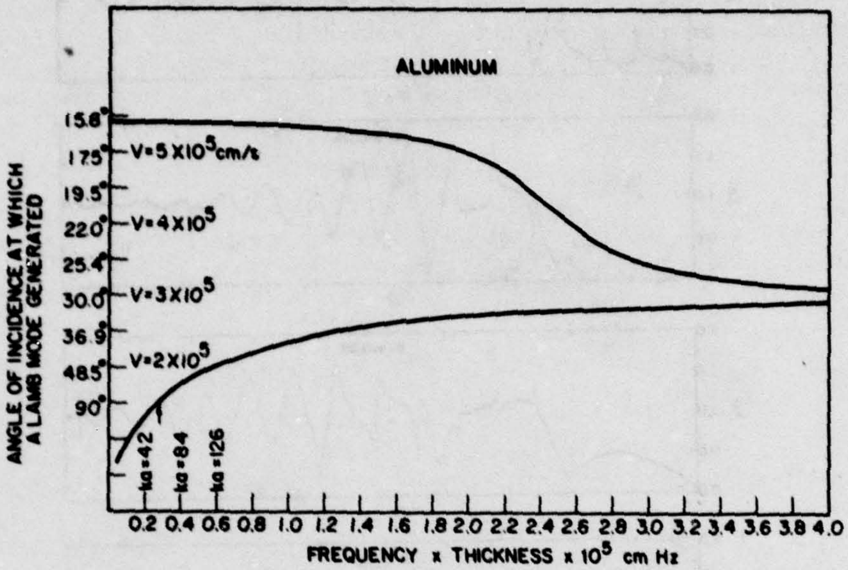

Fig. 35 – The angle of incidence at which the first symmetric and antisymmetric Lamb modes may be generated.

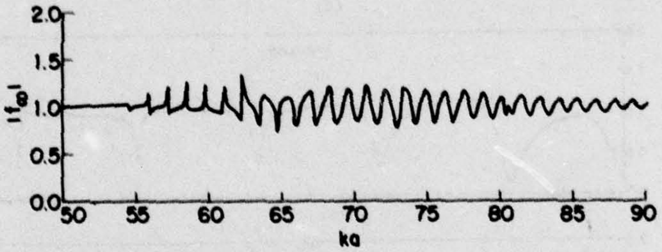

Fig. 36 – The form function vs ka over the range $50 \leq ka \leq 90$ for an for an aluminum shell with $b/a = 0.98$.

shells. Differences at $\Delta ka \simeq 1.3$ should begin to occur at lower *ka* values as thickness is increased. Fig. 37 shows the form function curves for aluminum cylindrical shells with $b/a =$ 0.99, 0.98, 0.96, 0.94, 0.92, 0.90, and 0.85. The above conclusions are verified in Fig. 37.

As thickness increases, the antisymmetric mode is seen to occur at lower *ka* values. The low velocity circumferential wave observed here in Figs. 27 and 28, and by the many others referenced earlier [12-15,25-27], is related to the first antisymmetric Lamb mode for a plate. The *ka* range over which it is generated depends on the thickness of the shell. The first symmetric mode is strongly generated on aluminum plates in the thickness region where it has a phase and group velocity ratio of $V/c = 3.7$. This is carried over to the shell case, where a circumferential wave having the properties of the first symmetric mode are observed at low *ka* on all thicknesses of shells from $0.85 \leqslant b/a \leqslant 0.99$. Closer spaced oscillations in $|f_\infty|$ vs *ka* are

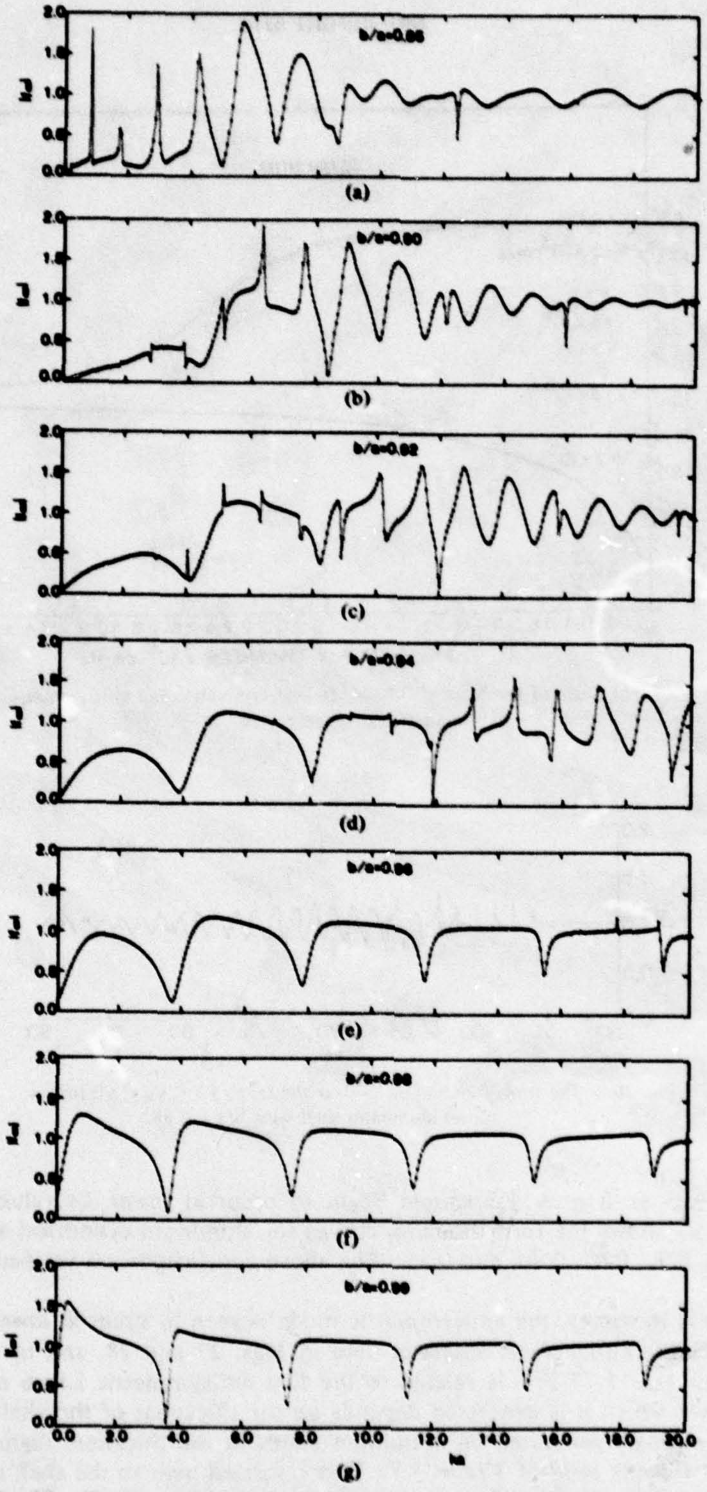

Fig. 37 – The form function vs ka over the range 0.2 ≤ ka ≤ 20 for aluminum shells with b/a values of (a) 0.85, (b) 0.90, (c) 0.92, (d) 0.94, (e) 0.96, (f) 0.98, and (g) 0.99.

also seen to occur at relatively lower ka values as shell thickness is increased. These oscillations are related to a circumferential wave with $c_p^*/c \simeq 1.3$. If one returns now to the Grigsby-Tajchman group velocity curves seen in Fig. 34b, the reason for the association of low frequency with low velocity and high frequency with high velocity in the literature becomes apparent. All the higher order Lamb modes in Fig. 34b are most strongly generated when their group velocity is $V_{gn} \simeq 1.8$. This is also the group velocity of the first symmetric mode at its region of strong excitation. Moreover, the same is true of all higher order antisymmetric modes (see Fig. 33). Thus the first symmetric mode and all higher order symmetric and antisymmetric modes cannot be distinguished from one another by measurement of group velocity alone, and these waves collectively have been identified as the fast circumferential wave. The particular mode generated depends on the shell thickness and frequency, but, as discussed earlier, practical considerations generally preclude isolation of the first symmetric mode. All of the measurements of a low velocity wave are related to the first antisymmetric mode, which for thin shells is generated at a higher frequency than the first symmetric mode but at a lower frequency than any of the higher order modes. In the empirical observations of circumferential waves, the wave related to the first antisymmetric mode is obtained at a frequency which depends on the thickness as described in Fig. 37.

Because of the slow speed of this wave, there is a greater time difference between successive traversals of the circumferential wave (a factor of 3 as compared to the faster waves); hence, this mode when present can be isolated at lower ka values than a mode traveling with a velocity 3 times higher. Thus in past pulse hydrophone measurements [12-15,27] low velocity corresponded to low frequency in the experimental observations. As frequency was increased it became possible to isolate higher velocity modes, all of which were strongly generated with the same group velocity; hence, high velocity corresponded experimentally to high frequency.

The circumferential wave related to the first symmetric mode is the only one of the "fast" circumferential waves whose amplitude approaches the amplitude of the specular reflection, and, while it is not practical to isolate it experimentally, its contribution to the steady state pressure or form function at low ka is apparent. As demonstrated in Fig. 33, it is possible to isolate the first symmetric mode by computation of the response of a shell to a short incident pulse. Computations similar to that seen in Fig. 33 are given in Figs. 38 and 39 for various shell thicknesses at various center frequencies. The purpose of these calculations is to demonstrate that the relative amplitude of the circumferential and specular contributions is a function of ka. In Figs. 38 the responses of three aluminum shells with thickness $b/a = 0.99$, 0.96, and 0.9 are presented. The center dimensionless frequency of the calculation is $k_0 a = 10$. A circumferential wave related to the first symmetric mode is seen in Fig. 38a ($b/a = 0.99$) and Fig. 38b ($b/a = 0.96$). The measured attenuation in these two cases is 0.50 Np/revolution (Fig. 38b) and 0.43 Np/revolution (Fig. 38a). In Fig. 38c the first antisymmetric mode is generated simultaneously with the symmetric mode. This figure demonstrates that the antisymmetric mode is in fact generated at lower frequency as thickness is increased, as predicted in the discussion of Fig. 37. It also shows that at the same $k_0 a$ the attenuation of the symmetric mode increases with increasing thickness, and finally it demonstrates that the large oscillations in $|f_\infty(\pi)|$ which appear with increasing thickness in Fig. 37 are due to the larger magnitude with which the antisymmetric mode is generated. The attenuation of the antisymmetric mode in Fig. 38c is 1.0 Np/revolution, which is much larger then that of the symmetric mode, but the magnitude of the first antisymmetric echo is more than 6 dB larger than that of the first symmetric echo.

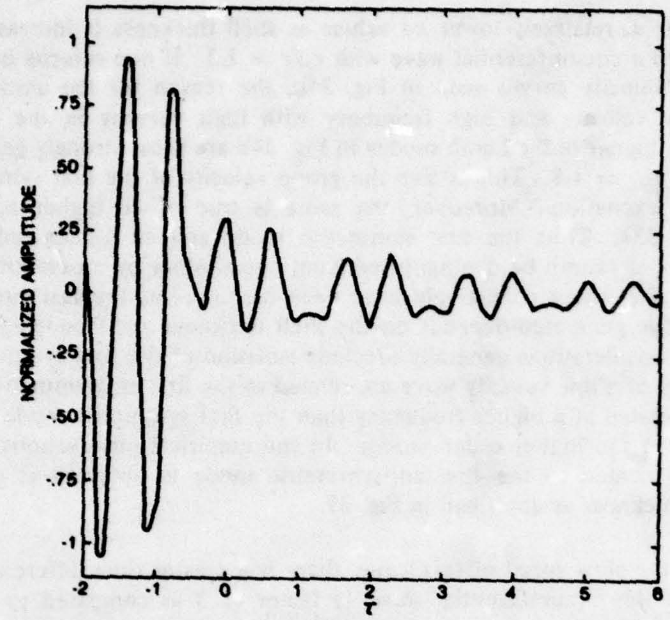

Fig. 38(a) – Computation of the echoes scattered by an aluminum shell at $k_oa = 10$; the shell thickness is $b/a = 0.99$.

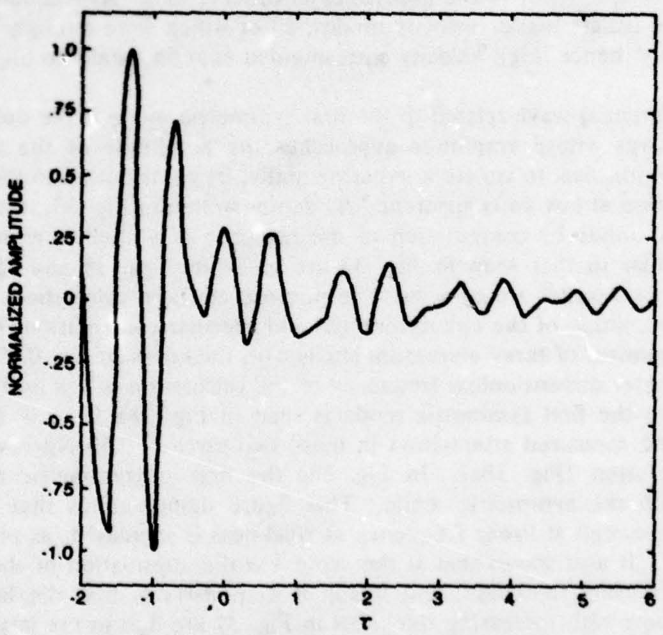

Fig. 38(b) – Computation of the echoes scattered by an aluminum shell at $k_oa = 10$; the shell thickness is $b/a = 0.96$.

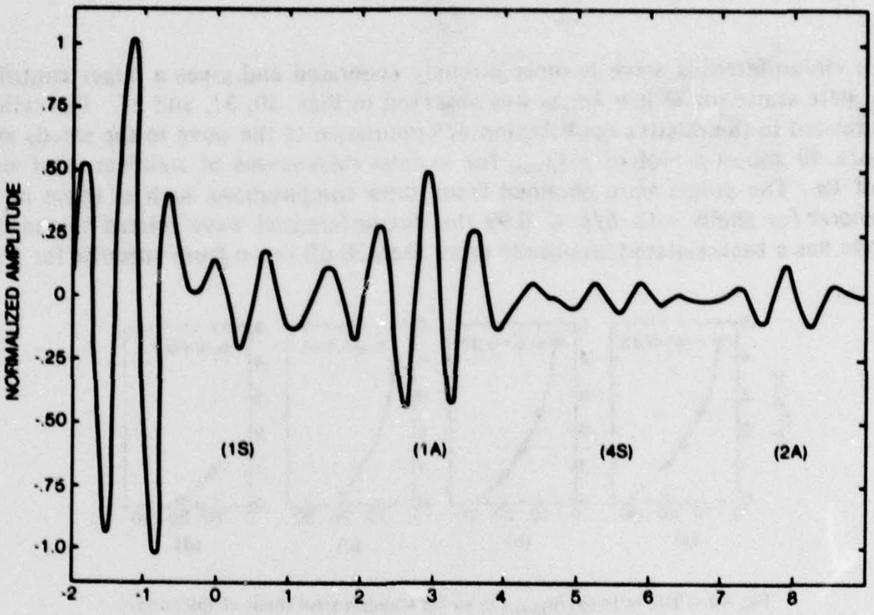

Fig. 38(c) – Computation of the echoes scattered by an aluminum shell at k_0a = 10; the shell thickness is b/a = 0.90.

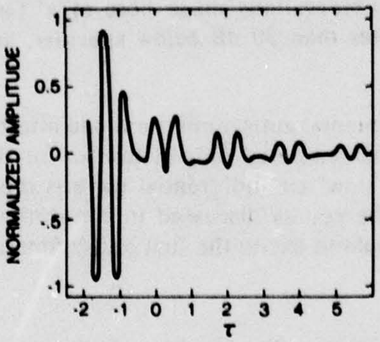

Fig. 39(a) – Computation of the echoes scattered by an iron shell b/a = 0.99 at a k_0a value of 11.

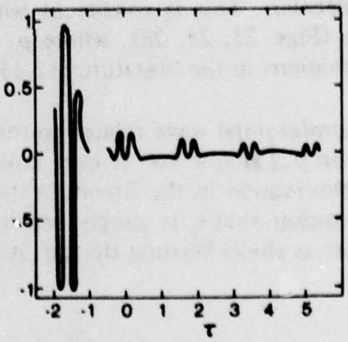

Fig. 39(b) – Computation of the echoes scattered by an iron shell b/a = 0.99 at a k_0a value of 20.

The responses of an iron shell with $b/a = 0.99$ at k_0a values of 11 and 20 are seen in Figs. 39(a) and 39(b) respectively. Here the attenuation is 0.46 Np/revolution at $k_0a = 11$ and 0.23 Np/revolution at $k_0a = 20$. Thus the attenuation decreases with higher frequency, an observation similar to that of Horton and Mechler [15], who observed this phenomenon at $ka \simeq 30$ for the wave identified here as the antisymmetric wave.

As may be observed in Fig. 38c, the attenuation of a circumferential wave is not necessarily a measure of its relative importance. If the ratio of the amplitude of the first circumferential echo, p_1, to the specular echo, p_{spec}, is taken from Figs. 39(a) and 39(b), the result obtained is $p_1/p_{\mathrm{spec}} = 0.2$ at $k_0a = 11$ and $p_1/p_{\mathrm{spec}} = 0.1$ at $k_0a = 20$. These ratios show that a particular circumferential wave is more strongly generated and gives a larger contribution to the steady state scattering at low *ka*, as was observed in Figs. 30, 31, and 37. The ratio p_1/p_{spec} is directly related to the relative contribution or importance of the wave to the steady state solution. Figure 40 shows a plot of p_1/p_{spec} for various thicknesses of stainless steel shells as a function of *ka*. The points were obtained from pulse computations such as those in Figs. 38-39. In general for shells with $b/a \leqslant 0.99$ the circumferential wave related to the first symmetric mode has a backscattered amplitude more than 20 dB down from specular for $ka > 20$.

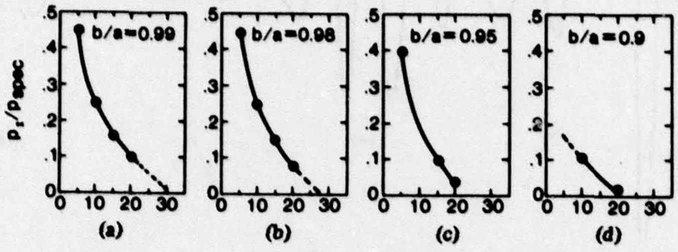

(a) (b) (c) (d)

Fig. 40 – The ratio (p_1/p_{spec}) vs ka for stainless steel shells of thicknesses (a) 0.99, (b) 0.98, (c) 0.95, and (d) 0.90.

For higher order modes generated above $ka = 20$, the ratio p_1/p_{spec} is more than 20 dB down from specular. This is consistent with the observations made here of a "fast" circumferential wave (Figs. 23, 25, 26), where p_1 is greater than 30 dB below specular, and with all reported observations in the literature [12-15,26].

The circumferential wave related to the fundamental antisymmetric mode also has its largest influence on $|f_\infty|$ at low *ka*. It can, however, be generated only at low *ka* for thick shells. The general observation in the literature that the "slow" circumferential wave is more strongly generated in thicker shells, is simply because of the results discussed in connection with Fig. 37, namely that as shells become thicker, it is possible to excite the first antisymmetric mode at lower *ka*.

The results considered here were for thin shells. Figures 33 and 34 show that as *fh* becomes larger, all the Lamb modes tend toward a final velocity $V \simeq 2.0c$. Since the phase velocity curves again level off for large *fh*, the Lamb modes are again strongly excited. Each higher order mode is first strongly excited at $V/c \simeq 3.7$ and then in the limit of a thick shell at $V/c \simeq 2.0$. Therefore it should be possible to find an intermediate frequency range at which a Lamb type mode is generated with $V/c \simeq 3.7$ simultaneously with a lower order mode which has reached its high frequency limit $V/c \simeq 2.0$. Such a situation is seen in Fig. 41. Here a schlerien visualization is made at an *fh* value of 11.2. The target is a 3.4 cm diameter aluminum cylinder with $b/a = 0.9$. This corresponds to $ka = 476$ and $kh = 47.6$. Simultaneous observation of circumferentials waves with $c_g^*/c = 3.7$ and $c_g^*/c = 2.0$ are seen. Figures 37 and 41 explain what has been referred to in the literature [12] as rare occurrances when slow and fast circumferential waves are observed simultaneously.

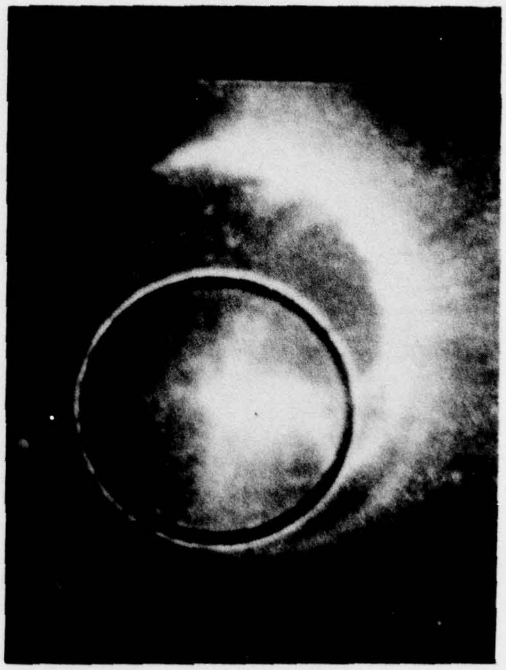

Fig 41 – Schlieren visualization of circumferential waves generated on an aluminum shell, with $b/a = 0.9$ at $k_o a = 476$.

VI. SUMMARY

The steady state acoustic response of infinitely long solid elastic cylinders and cylindrical shells can be exactly computed in terms of a normal mode series. For rigid cylinders the backscattered form function can be described in terms of the interference of a specularly reflected wave and a Franz type circumferential wave whose velocity and attenuation are related to the peaks and nulls in the form function. Solid metal cylinders in water exhibit this purely rigid behavior in the low ka region, after which region the form function is dominated by minima related to resonances in the individual normal modes. For cylinders made of metals whose shear and compressional wave speeds are greater than the wave speed of sound in water, the first resonance minimum observed is the (2,1) resonance. This occurs at $ka = 4.78$ for aluminum, and the ka value at which it occurs for other metals can be computed using aluminum as a reference.

The normal mode resonances are related to circumferential waves predicted by creeping wave theory. A mode resonates when its modal velocity is matched by the velocity of a circumferential wave. A single circumferential wave generates a given eigenfrequency in successive modes. The $(n, 1)$ resonances are related to the Rayleigh wave, and the (2,1), (3,1), and (4,1) modes are generated at ka values at which the cylinder circumference is 2, 3, or 4 Rayleigh wavelengths. Similarly the $(n, 2)$ resonances are related to the R_T-type whispering gallery mode and so on. The predominant circumferential waves in a given ka region can be predicted from the dominant resonance minima in $|f_\infty(\pi)|$. The "Rayleigh" wave was experimentally observed on aluminum in the predicted region.

The region of oscillations in $|f_\infty(\pi)|$ which begins at the position of the (2,1) resonance persists as $ka \to \infty$; however, in reality a frequency will be reached after which absorption must be included in the theory. In the resonance region ($ka > 4.78$ for aluminum) the scattering from the cylinder is made up of a rigid background part, on which the numerous resonances are superimposed. The resonance formalism of nuclear reaction theory is used to separate the exact normal mode series solution into rigid background and resonance terms, and resonance widths can be calculated.

For a thin cylindrical shell, the Franz wave does not measurably affect $|f_\infty(\pi)|$ even at low ka. This is consistent with soft rather than rigid scattering behavior, and it is demonstrated that as ka increases thin shells pass through three background regions. In the soft-background region at low ka the specular reflection is 180° out of phase with an incident pulse. This is followed by a region of intermediate background, and then a rigid-background region at which the specular and incident pulses are in phase and remain in phase as ka is further increased. Circumferential waves are isolated theoretically by applying fast Fourier transform techniques to the Fourier integral representing the echoes scattered, when a short acoustic pulse is incident on a shell. The relationship between the observed circumferential waves and the steady state form function shows that, for thin shells, the number of circumferential waves present, their velocity, and their relative significance can be obtained directly from the form function.

L. R. DRAGONETTE

Lamb theory for plates is utilized to predict the *ka* range of possible excitation of specific circumferential waves. A circumferential wave related to the first symmetric mode is generated for *ka* > 0, for all thin shells. A circumferential wave related to the first antisymmetric mode is generated at *ka* values which vary with thickness in a predictable way. As shell thickness is increased, circumferential waves related to all high order Lamb modes are strongly generated with the same group velocity. This accounts for observations reported previously in the literature and thought to be the observation of a single circumferential wave.

VII. REFERENCES

1. Lord Rayleigh, *Theory of Sound*, Dover (1945).
2. P. M. Morse, *Vibration of Sound*, McGraw-Hill (1936).
3. J. J. Faran, J. Acoust. Soc. Am. 23, 405-418 (1951).
4. R. Hickling, J. Acoust. Soc. Am. 34, 1582-1592 (1962).
5. R. Hickling, J. Acoust. Soc. Am. 36, 1124-1137 (1964).
6. L. D. Hampton and C.M. McKinney, J. Acoust. Soc. Am. 33, 664-673 (1961).
7. K. J. Diercks and R. Hickling, J. Acoust. Soc. Am. 41, 380-393 (1967).
8. W. G. Neubauer, R. H. Vogt, and L. R. Dragonette, J. Acoust. Soc. Am. 55, 1123-1129 (1974).
9. L. R. Dragonette, R. H. Vogt, L. Flax, and W. G. Neubauer, J. Acoust. Soc. Am. 55, 1130-1137 (1974).
10. H. D. Dardy, J. A. Bucaro, L. S. Scheutz, and L. R. Dragonette, J. Acoust. Soc. Am. 62, 1373-1376 (1977).
11. G. R. Barnard and C. M. McKinney, J. Acoust. Soc. Am. 33, 226-238 (1961).
12. K. J. Diercks, T. G. Goldsberry, and C. W. Horton, J. Acoust. Soc. Am. 35, 59-64 (1963).
13. C. W. Horton, W. R. King, and K. J. Diercks, J. Acoust. Soc. Am. 34, 1929-1932 (1962).
14. T. G. Goldsberry, J. Acoust. Soc. Am., 42, 1298-1305 (1967).
15. C. W. Horton and M. V. Mechler, J. Acoust. Soc. Am. 51, 295-303 (1972).
16. W. Franz, Z. Naturforsch 9a, 705-716 (1954).
17. G. N. Watson, Proc. Roy. Soc. (London) A95, 83-99 (1919).
18. W. Franz and K. Deppermann, Ann. Phys. 10, 361-373 (1952).
19. L. Flax, J. Acoust. Soc. Am. 62, 1502-1503 (1977).
20. H. Uberall, R. D. Doolittle, and J. V. McNicholas, J. Acoust. Soc. Am. 39, 564-578 (1966).
21. R. D. Doolittle, H. Uberall, and P. Ugincius, J. Acoust. Soc. Am. 43, 1-14 (1968).
22. O. D. Grace and R. R. Goodman, J. Acoust. Soc. Am. 39, 173-174 (1966).
23. W. G. Neubauer, J. Acoust. Soc. Am. 44, 298-299 (1968).
24. M. L. Harbold and B. N. Steinberg, J. Acoust. Soc. Am. 45, 592-603 (1969).
25. R. E. Bunney, R. R. Goodman, and S. W. Marshall, J. Acoust. Soc. Am. 46, 1223-1233 (1969).
26. W. G. Neubauer, J. Acoust. Soc. Am. 45, 1134-1144 (1969).
27. W. G. Neubauer and L. R. Dragonette, J. Acoust. Soc. Am. 48, 1135-1149 (1970).
28. D. Brill and H. Uberall, J. Acoust. Soc. Am. 50, 921-939, (1971).
29. K. Dransfeld and E. Salzmann, in *Physical Acoustics, Vol. VII*, edited by Warren P. Mason and R. N. Thruston, Academic Press (1970).
30. W. G. Neubauer and L. R. Dragonette, J. Appl. Phys. 45, 618-622 (1974).
31. L. A. Scheutz and W. G. Neubauer, J. Acoust. Soc. Am. 62, 513-517 (1977).
32. L. Flax and W. G. Neubauer, J. Acoust. Soc. Am. 61, 307-312 (1977).
33. R. E. Bunney and R. R. Goodman, J. Acoust. Soc. Am. 53, 1658-1662 (1973).
34. R. H. Vogt, L. Flax, L. R. Dragonette, and W. G. Neubauer, J. Acoust. Soc. Am. 57, 558-561 (1975).

35. G. V. Frisk and H. Uberall, J. Acoust. Soc. Am. 59, 46-54 (1976).
36. W. G. Neubauer, J. Appl. Phys. 44, 48-55 (1973).
37. H. L. Bertoni and T. Tamir, Appl. Phys. 2, 157-172 (1973).
38. E. K. Sittig and C. A. Coquin, J. Acoust, Soc. Am. 48, 1150-1159 (1970).
39. I. A. Viktorov, *Rayleigh and Lamb Waves*, Plenum Press (1967).
40. M. C. Junger and D. Feit, *Sound Structures and Their Interactions*, M.I.T. Press (1972).
41. R. H. Vogt and W. G. Neubauer, J. Acoust. Soc. Am. 60, 15-22 (1976).
42. S. deBenedetti, *Nuclear Interactions*, Wiley (1964).
43. D. G. Tucker and N. J. Barnickle, J. Sound Vib. 9, 393-397 (1969).
44. P. Ugincius and H. Uberall, J. Acoust. Soc. Am. 43, 1025-1035 (1968).
45. L. R. Dragonette, J. Acoust. Soc. Am. 51, 920-935 (1972).
46. D. J. Shirley and K. J. Diercks, J. Acoust. Soc. Am. 48, 1275-1282 (1970).
47. J. D. Murphy, E. D. Breitenback, and H. Uberall, J. Acoust. Soc. Am. (to be published).
48. H. Lamb, Proc. Roy. Soc. (London) 93, 114-128 (1917).
49. D. C. Worlton, J. Appl. Phys. 32, 967-971 (1961).
50. M. F. Osborne and S. D. Hart, J. Acoust. Soc. Am. 17, 1-18 (1945).
51. T. N. Grigsby and E. J. Tajchman, IRE Trans. UE-8, 26-33 (1961).

Appendix A

LIST OF SYMBOLS

a - the radius of the target
a_{ij} - matrix elements defined in Ref. 32
$\mathbf{A}$ - the vector potential
b - the inner radius of a cylindrical shell
B_n - a coefficient in Eq. 50b
c - the velocity of sound in water
c_p^F - the phase velocity of the Franz wave
c_g^F - the group velocity of the Franz wave
$c_n(ka)$ - the modal phase velocity for the n^{th} normal mode
$c_n^g(ka)$ - the modal group velocity for the n^{th} normal mode
$c_l(ka)$ - the phase velocity of the l^{th} R-type circumferential wave
$c_l^g(ka)$ - the group velocity of the l^{th} R-type circumferential wave
c_R - the phase velocity of the Rayleigh or R_1 circumferential
c_R^g - the group velocity of the Rayleigh or R_1 circumferential wave
c_L - the longitudinal wave velocity in a material
c_T - the shear wave velocity in a material
$c_p^{\bullet}$ - the phase velocity of a circumferential wave in a cylindrical shell
$c_g^{\bullet}$ - the group velocity of a circumferential wave in a cylindrical shell
C_n - a coefficient in Eq. 50a
d - distance
$D_n^{(1)}(ka)$ - A 2-by-2 matrix defined in Eq. 1a
$D_n^{(2)}(ka)$ - A 2-by-2 matrix defined in Eq. 1a
f_∞ - the far field form function
f_∞^R - the far field form function for a rigid cylinder
f_n - the n^{th} partial wave or n^{th} modal contribution to the form function
f - frequency
f_o - the center frequency of an incident pulse
fh - the frequency thickness product
$(fh)_n$ - the dimensionless frequency thickness parameter, $(fh)_n = fh/c_T$
$g_i(ka)$ - the spectrum of an incident pulse
$g_s(ka)$ - the spectrum of a scattered echo
$G_n(Z)$ - defined in Eq. 3
$G_n^R(Z)$ - the expression to which $G_n(Z)$ reduces when the target is a rigid cylinder
h - the thickness of a cylindrical shell
$H_n(Z)$ - the Hankel function of the first kind (order n, argument Z)
$H_n^{(2)}(Z)$ - the Hankel function of the second kind (order n, argument Z)
$H_n'(Z)$ - the derivative of the Hankel function of the first kind with respect to its argument
$H_n^{(2)'}(Z)$ - the derivative of the Hankel function of the second kind with respect to its argument

$J_n(Z)$ - the Bessel function (order n, argument Z)
$J'_n(Z)$ - the derivative of the Bessel function with respect to its argument
k - the wavenumber in water given by $k = 2\pi/\lambda$
k_L - the longitudinal wavenumber in a material
k_T - the shear wavenumber in a material
ka - the dimensionless frequency variable, $ka = 2\pi a/\lambda$
$(ka)_o$ - the center dimensionless frequency of a pulse in water
$(ka)_{peak}$ - the ka value at which a peak in $|f_\infty|$ occurs
l - an integer, $l = 1, 2, \ldots$, used to number the eigenfrequencies of a given mode
L_n - defined in Eq. (1a)
n - an integer, $n = 1, 2, \ldots$, used to number the normal modes
$p_i(\tau)$ - an incident acoustic pulse
p_o - the incident plane-wave amplitude
p_1 - the pressure amplitude of the first backscattered circumferential echo
$p_s(\theta)$ - the steady state scattered acoustic pressure at the bistatic angle θ .
p_{spec} - the pressure amplitude of the specular reflec[illegible]
q_l - the zeroes of the first derivatives of the Airy function
Q_n - defined in Eq. 54
r - the range or distance between the scatterer and the field point
R_l - the l^{th} order Rayleigh-type circumferential wave
s_n - defined in Eq. 40
S_n - the elastic scattering function defined by $S_n \equiv \exp(2i\,\delta_n)$
$S_n^{(R)}$ - the rigid body scattering function defined as $S_n^{(R)} \equiv \exp(2\,i\,\xi_n)$
t - time
u - the particle displacement
V - the phase velocity of a Lamb wave
V_g - the group velocity of a Lamb wave
V_n - dimensionless Lamb phase velocity given by $V_n = V/c^T$
V_{gn} - dimensionless Lamb group velocity givey by $V_{gn} = V_g/c_T$
$Y_n(Z)$ - the Neumann function (argument Z, order n)
$Y'_n(Z)$ - the derivative of the Neumann function with respect to its argument
Z - short-hand form for the dimensionless frequency variable $Z \equiv ka$
Z_n - the dimensionless frequency at a resonance, $Z \equiv (ka)_n$
Z_{pole} - the Z value at which a resonance pole in the scattering function S_n occurs
Z_{zero} - the Z value at which a resonance zero in the scattering function S_n occurs
z_1 - defined in Eq. 37a
z_2 - defined in Eq. 37b
α_l^F - the attenuation coefficient for the Franz wave
α_R - the attenuation coefficient for the Rayleigh or R_1 circumferential wave
α'_R - the dimensionless attenuation coefficient for the R_1 circumferential wave
α^* - the attenuation coefficient for a circumferential wave in a shell
β_n - coefficient in the Taylor series expansion (Eq. 42b)
Γ_n - the width of a resonance, given by $\Gamma_n = -2s_n/\beta_n$
δ_n - scattering phase shift for the elastic scattering function
Δd - change in distance
Δka - change in ka

Δt - change in time
$\Delta \tau$ - change in the dimensionless time parameter
Δn - defined in Eq. 39
ϵ_n - the Neumann factor $\epsilon_n = 2,\ n = 0;\ \epsilon_n = 1,\ n > 0$
θ - the polar angle
θ_i - the incidence of angle of a plane wave
λ - the wavelength of sound in water
λ_R - the wavelength of the Rayleigh wave on a flat surface
λ^* - the wavelength of a circumferential wave
ν - a complex variable
ζ_n - the phase shifts for the rigid scattering function
ρ - the density of water
ρ_s - the density of the target material
τ - the dimensionless time parameter $\tau \equiv \dfrac{ct - a}{r}$
ϕ - the azimuthal angle
Ψ - a scalar potential
ω - the angular frequency, $\omega = 2\pi f$

Appendix B

THE MEASUREMENT SYSTEMS

1. Pool facility measurement system

Pulse hydrophone measurements were obtained with the system described in Fig. B1. The source/receiver transducers are lead-zirconate-titanate immersion search units, with active elements 3.175 cm square and resonant frequencies of from 400 kHz to 1.5 Mhz. The water tank is an aquarium 76 cm by 183 cm by 76 cm deep. The targets were 30-cm-long solid cylinders and cylindrical shells made of aluminum and stainless steel. A Panametrics model 5055 PR pulse/receiver allowed a single transducer to act as both source and receiver, so that a monostatic geometry was exactly maintained. External triggering was generated by a Hewlett Packard model 214A pulse generator. A pulse repetition rate of 10 ms was chosen, so that all reverberation from the tank boundaries would decay beneath the system sensitivity before the pulser generated the next acoustic pulse. The driving pulse produced by the Model 5055 PR pulser/receiver is a rectangular pulse, which causes the transducers to ring at their fundamental and overtone frequencies. The pulser/receiver unit internally separates the driving pulse and received acoustic echoes (acts as a transmit/receive switch) so that a monostatic geometry can be exactly maintained by having a single transducer perform both tasks. The received signal is filtered by a Krohn-Hite model 3202 electronic filter so that either the fundamental or the harmonic frequencies may be isolated. The filtered signal is then displayed on a model 545A Tektronix oscilloscope, from which a photographic representation can be obtained. The filtered signal may also be digitized using a Biomation model 8100 analog-to-digital converter, and analyized and stored using a Digital Equipment PDP-11 computer. Digital signals are stored on

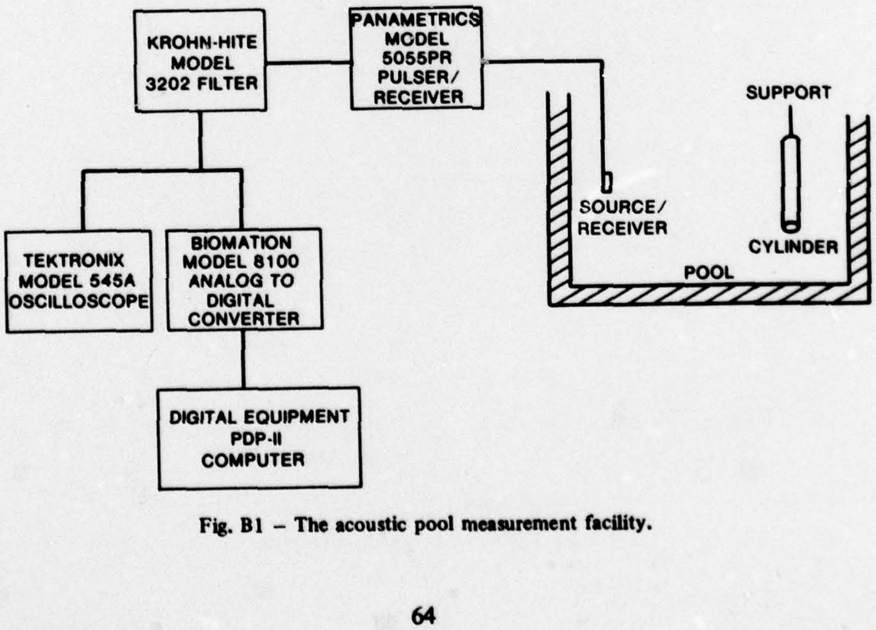

Fig. B1 – The acoustic pool measurement facility.

magnetic tape for future analysis or may be analized in near real time. The digitized signal is displayed on a Tektronix 4010 graphic terminal, and a hard copy (such as that seen in Fig. 15) can be obtained from the copy unit or the digitized signal can be plotted on a Versatic plotting unit (such as seen in Fig. 14).

Amplitude measurements are made directly with the oscilloscope by using a Tektronix type-W plug-in unit; they may also be made by using the computer software in which the computer seeks out peaks in the digital representation of the pulse. Amplitude measurements by either means were demonstrated accurate to within 2 percent of exact calculation where such computations were possible [8-10,32].

2. Schlieren visualization system

Schlieren visualization gives an immediate look in one plane at the entire scattered field around the acoustic target. It is especially useful in the case of beam aspect illumination of long cylindrical targets, which is a two dimensional problem. The schlieren system used here is described schematically in Fig. B2. The light source, lenses, and tank are mounted on a 183-cm-long Gaertner optical bench. Special carriages allow continuously variable motion in three dimensions for the light source and the stop. A General Radio Stroboslave model 1539A is the light source. A condensing lens focuses the light from the source, to a small aperture at A in Fig. B2. This aperture is an effective point source. The lens at B is one focal length from A and forms a parallel beam which travels through the water tank to the lens at C. The tank has specially constructed plate-glass sides to avoid any distortion of the parallel beam. The critical parameter in the placing of the lens at point C is the focal length of this lens. The lens is placed one focal length from the plane of the acoustic experiment to be visualized. In the case described here the focal length of the lens is 25 cm. The final steps in the creation of the schlieren system described in Fig. B2 are the mounting of a 0.05-cm-diameter stop at a distance of 25 cm (one focal length) beyond the lens at C. The position of the stop is labeled D in the figure. A Fairchild model TC-177 television camera is mounted directly beyond the stop.

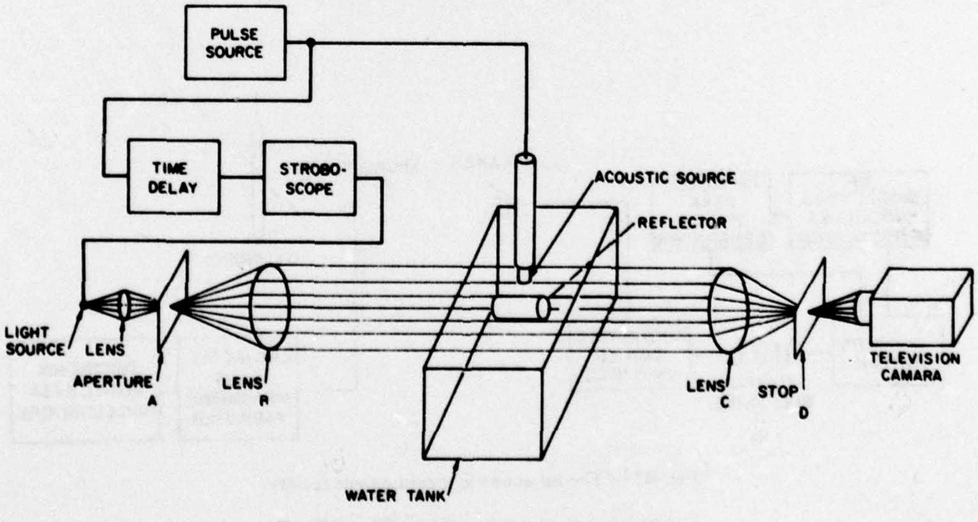

Fig. B2 – The schlieren visualization system.

In the system described in Fig. B2 all the light passing through the aperture is intercepted by the stop, at position D, in the absence of an acoustic experiment. When, however, an acoustic field exists, the parallel light rays passing through the acoustic field are diffracted, miss the stop, and are detected by the television camera. The camera is connected to a Panasonic videotape unit on which observations may be stored and to a televison monitor from which the schlieren images (Figs. 41 and 29) were obtained with a Polaroid camera. The acoustic transducers are as described above for the pulse hydrophone measurements, with resonant frequencies of from 1 MHz to 8 MHz suitable for schlieren studies in this system. The driving signal is a gated sine wave produced by a model PG650-C Arenberg pulsed oscillator. The external trigger and time delay are provided by a Hewlett Packard model 214A pulse generator. This unit triggers the light source and the pulsed oscillator, allowing delays of from 0 to 100 ms between the triggering of the light and sound sources. This delay makes possible the time sequence pictures seen in Fig. 29.

3. Air system

The air acoustics system is seen schematically in Fig. B3. The experimental technique in air is similar to that in water, but the sources, receivers, and frequencies are different. The air acoustics system allows the simulation of rigid boundary conditions. The acoustic system employs LTV electrostatic sources 5.08 cm and 15.24 cm in diameter to produce the incident acoustic pulses. The receivers are Bruel and Kjaer 0.635-cm-diameter microphones. The targets are hung in a large room 9 m by 30 m by 15 m high. Variable length gated sine wave pulses are produced by using a Hewlett Packard model 214A pulse generator and Sanders switch to gate the continuous sine wave output of a Hewlett Packard model 5110 frequency synthesiser. The gated sine wave output is amplified by a Krohn-Hite model DCA 50 amplifier whose output drives the electrostatic speaker. The signal received by the 0.635-cm-diameter microphone is filtered by a Krohn-Hite model 312 bandbass filter and amplified with a Bruel and Kjaer type 2107 frequency analyzer. The microphone is mounted on a stand and placed by hand at the desired aspect angle. A positioning of ± 2° is possible in the air measurements. The received signal is amplified and analyzed by the same equipment as described for the pool facility in section 1.

Fig. B3 – The air acoustic measurement facility.

Appendix C

TABLE OF CONSTANTS

Material	C_L (10^5 cm/s)	C_T (10^5 cm/s)	ρ (g/cc)
air	00.343	0.000	0.00
aluminum	06.370	3.120	2.17
aluminum oxide	10.700	6.300	3.92
iron	05.950	3.240	7.70
stainless steel	05.5940	3.106	7.90
water	01.493	0.000	1.00